nature communications

Article

https://doi.org/10.1038/s41467-024-53002-0

CHIP ameliorates nonalcoholic fatty liver disease via promoting K63- and K27-linked STX17 ubiquitination to facilitate autophagosome-lysosome fusion

Received: 10 September 2023

Accepted: 26 September 2024

Published online: 02 October 2024

Check for updates

Hyunjin Rho[1], Seungyeon Kim[1], Seung Up Kim[2], Jeong Won Kim[3], Sang Hoon Lee[4,5], Sang Hoon Park[6], Freddy E. Escorcia[7], Joon-Yong Chung[7] & Jaewhan Song[1]

The fusion of autophagosomes and lysosomes is essential for the prevention of nonalcoholic fatty liver disease (NAFLD). Here, we generate a hepatocyte-specific CHIP knockout (H-KO) mouse model that develops NAFLD more rapidly in response to a high-fat diet (HFD) or high-fat, high-fructose diet (HFHFD). The accumulation of P62 and LC3 in the livers of H-KO mice and CHIP-depleted cells indicates the inhibition of autophagosome-lysosome fusion. AAV8-mediated overexpression of CHIP in the murine liver slows the progression of NAFLD induced by HFD or HFHFD feeding. Mechanistically, CHIP induced K63- and K27-linked polyubiquitination at the lysine 198 residue of STX17, resulting in increased STX17-SNAP29-VAMP8 complex formation. The STX17 K198R mutant was not ubiquitinated by CHIP; it interfered with its interaction with VAMP8, rendering STX17 incapable of inhibiting steatosis development in mice. These results indicate that a signaling regulatory mechanism involving CHIP-mediated non-degradative ubiquitination of STX17 is necessary for autophagosome-lysosome fusion.

Nonalcoholic fatty liver disease (NAFLD) is characterized by substantial lipid accumulation in the liver, a condition that is strongly associated with metabolic syndromes, such as obesity and type 2 diabetes mellitus (T2DM)[1,2]. Based on this significant association between NAFLD and metabolic dysfunctions, new nomenclature such as metabolic dysfunction associated fatty or steatotic liver disease (MAFLD or MASLD) was recently proposed[3]. Nevertheless, NAFLD encompasses a range of conditions, from simple steatosis to non-alcoholic steatohepatitis (NASH). NASH is a dynamic manifestation of NAFLD, characterized by the presence of steatosis, hepatocyte ballooning, inflammation, and fibrosis[4]. These pathological features can lead to the development of cirrhosis and hepatocellular carcinoma[5]. NAFLD represents a stage wherein the impaired liver can potentially be restored to a healthy state through diet and exercise[6,7]. Nevertheless, the absence of long-term sustainability in diet and exercise management and the intricate heterogeneity of NASH present significant challenges in conducting pharmacotherapeutic trials and identifying effective biomarkers for treatment[8].

[1]Department of Biochemistry, College of Life Science and Technology, Institute for Bio-medical Convergence Science and Technology, Yonsei University, Seoul, Republic of Korea. [2]Department of Internal Medicine, College of Medicine, Yonsei University, Seoul, Republic of Korea. [3]Department of Pathology, Kangnam Sacred Heart Hospital, Hallym University College of Medicine, Seoul, Republic of Korea. [4]Department of Digital Health, Samsung Advanced Institute for Health Sciences and Technology, Sungkyunkwan University, Seoul, Republic of Korea. [5]GENINUS Inc, Seoul, Republic of Korea. [6]Department of Internal Medicine, Kangnam Sacred Heart Hospital, Hallym University College of Medicine, Seoul, Republic of Korea. [7]Molecular Imaging Branch, Center for Cancer Research, National Cancer Institute, National institutes of Health, Bethesda, MD, USA. e-mail: jso678@yonsei.ac.kr

Macroautophagy (hereafter referred to as autophagy) involves the degradation of cellular components via fusion of autophagosomes and lysosomes. It is widely recognized for its regulatory function in NAFLD advancement[9,10]. Autophagosomes fuse with lysosomes via soluble N-ethylmaleimide-sensitive factor activating protein receptor (SNARE) complexes, tethering proteins, and Rab GTPases to achieve cellular component degradation and recycling[11]. The STX17-SNAP29-VAMP8 complex is one of the most well-known SNARE complexes that induces autophagosome-lysosome fusion. STX17 is located on the autophagosome membrane, where it binds to the intermediate protein SNAP29, which then binds to VAMP8 on the lysosome[12,13]. While the effects of SNAP29 and VAMP8 on the regulation of NAFLD progression remain unclear[14], STX17 is relatively more explored. For example, proteasomal degradation of STX17 via increased homocysteinylation and ubiquitination leads to NALFD progression[15]. Furthermore, increased acetylation of PACER induces an interaction between STX17 and the HOPS complex[16], and the loss of SRSF3 leads to ubiquitination-dependent proteasomal degradation of STX17, which decreases lipophagy under free fatty acid (FFA)-rich conditions[17]. Although these studies have investigated the post-translational modification-mediated proteasomal degradation of STX17, the involvement of non-degradative ubiquitination of STX17 in regulating SNARE complex formation under NAFLD is unknown. In addition, as these studies were conducted in wild-type mice with induced metabolic syndromes or knockout of STX17 regulators, such as PACER, confirming the actual regulatory effects of STX17 in vivo is challenging.

CHIP is an E3 ligase that participates in protein degradation and cell signaling pathways via ubiquitinating multiple target substrates[18,19]. These substrates have been implicated in tumorigenesis[20–22], aging[23–25], and metabolic syndromes[26–29]. CHIP is also known to regulate lysosomal and autophagy-related gene transcription via regulation of TFEB[30], and regulates mitophagy via interaction with PARKIN[31]. However, most of these investigations were conducted in vitro or in whole-body CHIP-null mice. As CHIP-null mice exhibit perinatal lethality and dwarfism[32,33], eliminating the possibility of systemic malfunctions affecting specific pathways in the organs is challenging. Therefore, the use of whole-body CHIP-null mice or cellular systems substantially limits the ability to accurately interpret CHIP function in specific organs, such as the liver.

In this study, we examined the direct function of CHIP in regulating the non-degradative ubiquitination of STX17 in the K198 residue via K63- and K27-linkages, which increased the interaction with VAMP8, consequently leading to increased lipophagy in the liver. The livers of patients and mice with NAFLD exhibited significant downregulation of CHIP and STX17 expression at the physiological level. The decreased expression of CHIP correlated with the K63- and K27-linked ubiquitination of STX17. Ultimately, the K198 residue (K197 residue in mice) of STX17 was ascertained to play a significant role in mitigating NAFLD progression in living organisms. Furthermore, the pronounced reversal of NAFLD progression via AAV8-mediated CHIP overexpression indicated the potential of this mechanism as a viable therapeutic target.

Results

The expression of CHIP is down-regulated in the liver specimens of NASH patients and liver tissues of mice fed high-fat diet (HFD) or high-fat, high-fructose diet (HFHFD)

The transcript level of CHIP in NASH patients was analyzed from the Gene Expression Omnibus database (http://www.ncbi.nlm.nih.gov/geo/, GSE89632)[34]. Next, we assessed the immunoreactivity of CHIP in liver biopsies taken from patients with NASH, as well as normal liver tissues. The expression of CHIP was reduced in NASH tissue specimens compared with that in normal liver tissues (Fig. 1a, b). To further investigate the role of CHIP in NAFLD progression, mice were fed HFD or HFHFD to induce simple steatosis or NASH, respectively. We observed that the protein levels of CHIP were significantly downregulated as NASH progressed in mouse livers, specifically in hepatocytes (Fig. 1c–f). Overall, the expression levels of liver CHIP seem to be reduced with the progression of metabolic syndromes.

CHIP promotes the lipophagy pathway via facilitating autolysosome formation

Changes in the autophagy signaling network caused by prolonged metabolic stress are known to regulate NASH[35]. As CHIP has also been reported to be involved in autophagy pathways, we examined its function in relation to lipophagy, a form of autophagy that selectively degrades intracellular lipid droplets. The lipid droplet accumulation increased in cells lacking CHIP (Fig. 2a). Alternatively, treatment with an autophagosome and lysosome fusion blocker, bafilomycin A1[36], inhibited the effects of lipid degradation in CHIP-overexpressing cells (Fig. 2b), indicating CHIP as a regulator of the lipophagy pathway. Next, we examined the regulatory effects of lipophagy via expressing CHIP mutants, H260Q and K30A, which are known to be defective in E3 ligase and chaperone binding activities, respectively. Lipid droplet degradation via CHIP was inhibited only when H260Q was overexpressed (Fig. 2c), indicating that lipophagy induction via CHIP may require ubiquitination-dependent mechanisms, and not chaperone-mediated autophagy[37]. Using tandem RFP-GFP-LC3 to measure autophagic flux, we monitored autophagy activation in an oleic acid (OA)-rich environment. RFP-GFP-LC3 displays yellow puncta in the autophagosome due to the simultaneous expression of RFP and GFP, whereas it displays red puncta in the lysosome due to the loss of GFP activity caused by the acidic pH of the lysosome[38]. CHIP-depleted cells exhibited increased yellow puncta, indicating that autophagosome deposition was induced via their inhibition of lysosome fusion (Fig. 2d and Supplementary Fig. 1a). In contrast, more red puncta were observed when CHIP WT and K30A mutants were overexpressed in the cells (Fig. 2e and Supplementary Fig. 1b). Overexpression of H260Q prevented cells from inducing autophagy, corroborating data demonstrating its incapacity to induce lipophagy (Fig. 2c, e). In accordance with these findings, downregulation of CHIP resulted in the accumulation of P62 and LC3-II, suggesting the inhibition of late-stage autophagy (Fig. 2f). In contrast, autophagy activation was observed in CHIP-overexpressing cells, as evidenced by increased degradation of p62 and increased levels of LC3-II (Fig. 2g). This activation was effectively inhibited via bafilomycin A1 administration. Finally, CHIP exhibited co-localization with lipid droplets (h1), decreasing the lipid droplets near highly expressed regions of CHIP (h2; Fig. 2h). This suggests a potential direct involvement of CHIP in the lipophagy process. Increased lipid droplet levels may lead to lipotoxicity, resulting in increased inflammation- and fibrosis-related gene expressions[39,40]. Accordingly, inflammation- and fibrosis-related gene expression levels were increased in CHIP-depleted cells (Supplementary Fig. 1c-d), while they were decreased under CHIP overexpression (Supplementary Fig. 1e-f). Contrastingly, H260Q overexpression alone did not prevent these effects, indicating that the E3 ligase activity of CHIP may be necessary. Overall, CHIP may play a role in the regulation of fusion between autophagosomes and lysosomes, potentially through its function as an E3 ligase rather than its ability to interact with chaperones.

HFD exacerbates liver steatosis, inflammation, fibrosis, and metabolic syndromes in hepatocyte-specific CHIP knockout (H-KO) mice

To investigate the role of CHIP in the regulation of autophagy in vivo, H-KO mice were generated (Supplementary Fig. 2a). Weight gain, food intake, or phenotypic changes in adipose tissues, including subcutaneous fat (SubQ), epididymal fat (Epi), and brown adipose tissue (BAT) showed no differences (Supplementary Fig. 2b-f) when CHIP flox/flox control (WT) and H-KO mice were fed

https://doi.org/10.1038/s41467-024-53002-0

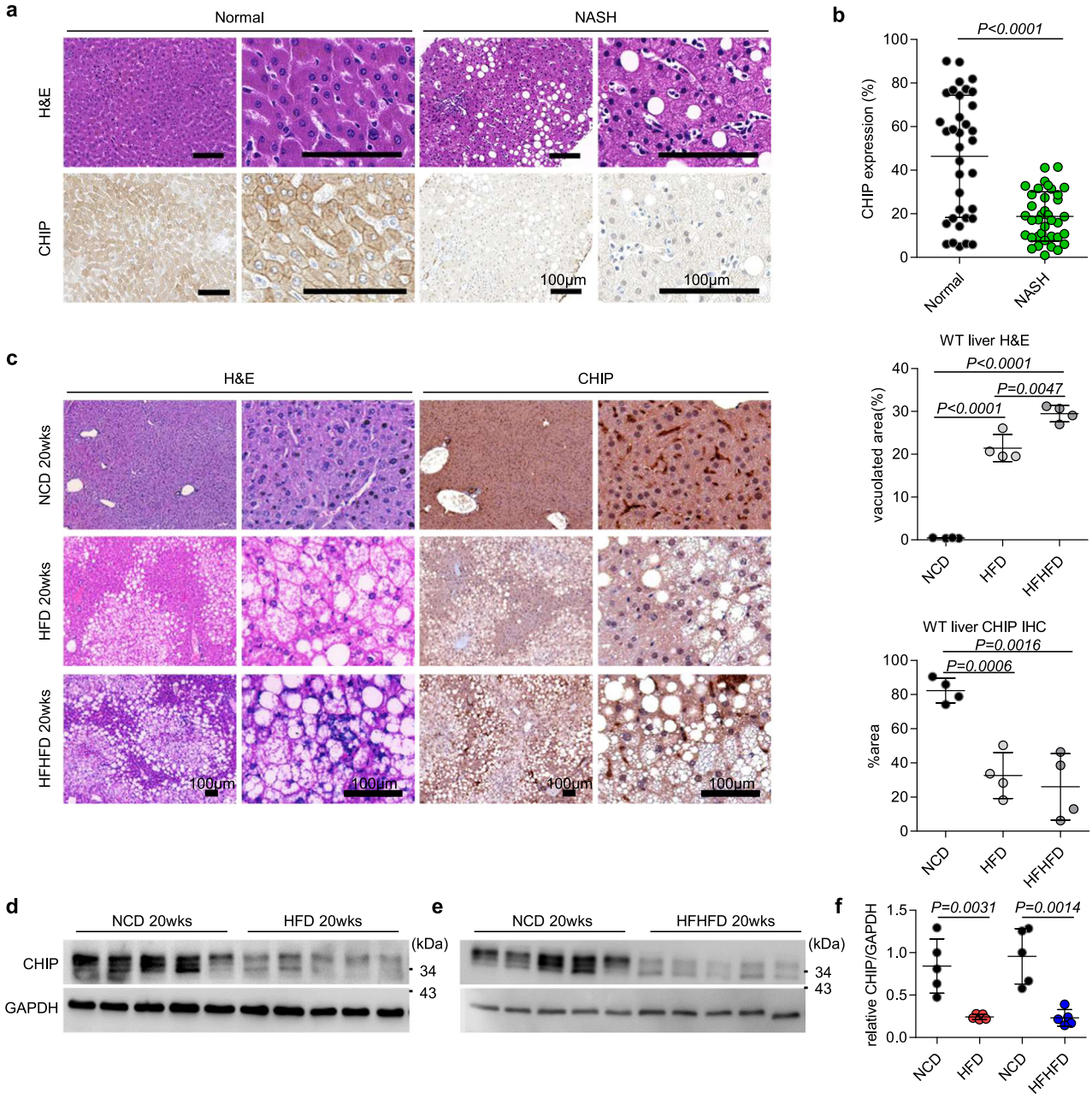

Fig. 1 | The expression of CHIP is down-regulated in the liver specimens of NASH patients and liver tissues of mice fed high-fat diet (HFD) or high-fat, high-fructose diet (HFHFD). Immunohistochemical detection of CHIP protein in human normal and nonalcoholic fatty liver specimens. **a** Representative immunohistochemical staining images for CHIP in formalin-fixed paraffin-embedded (FFPE) liver tissues. H&E staining of FFPE human liver samples diagnosed as normal and NASH are shown at top of the image. Scale bar shown is 100 μm. **b** A dot plot of CHIP expression in human liver samples (Normal, n = 35; NASH, n = 37). CHIP expression was significantly lower in NASH specimens compared to normal liver tissues. Mice were fed a NCD, HFD, or HFHFD for 20 weeks (n = 5). **c** Representative images of liver sections stained with H&E and anti-CHIP antibody as indicated. **d**–**f** Western blotting and quantification of the liver samples. Data are presented as individual data points, mean ± SD is assessed by unpaired two-tailed *t*-test. NCD, normal chow diet; HFD high-fat diet, HFHFD high-fat high-fructose diet.

a normal chow diet (NCD) for 32 weeks (Supplementary Fig. 3a). Morphological and histochemical liver analyses, including steatosis, fibrosis, macrophage infiltration, and protein expression of autophagy markers P62 and LC3, revealed no differences between WT and H-KO mice (Supplementary Fig. 3b-h). The transcript levels related to inflammation and fibrosis did not change (Supplementary Fig. 3i-j). Furthermore, analyses of hepatic triglyceride (TG), hepatic total cholesterol (TC), and serum factors, including alanine transaminase (ALT), and aspartate aminotransferase (AST), TG, TC, very low-density lipoprotein (VLDL), FFA, high-density lipoprotein (HDL), and low-density lipoprotein (LDL) levels, showed no difference between WT and H-KO mice (Supplementary Fig. 3k-n). To further examine the gene expression patterns in WT and H-KO mice with NCD, we performed bulk RNA sequencing (RNAseq). The gene set enrichment analysis (GSEA) data indicated that there were no significant differences in metabolic pathways including glycolysis, gluconeogenesis, β-oxidation, fatty acid synthesis, lipogenesis, mitochondrial biogenesis, cell growth, autophagy, inflammation, and fibrosis between WT and H-KO mice with NCD (Supplementary Fig. 3o-p). Moreover, the top ten pathways that were differentially regulated between WT and H-KO mice included kidney mesenchyme morphogenesis, neural plate pattern specification, and embryonic development, which were

https://doi.org/10.1038/s41467-024-53002-0

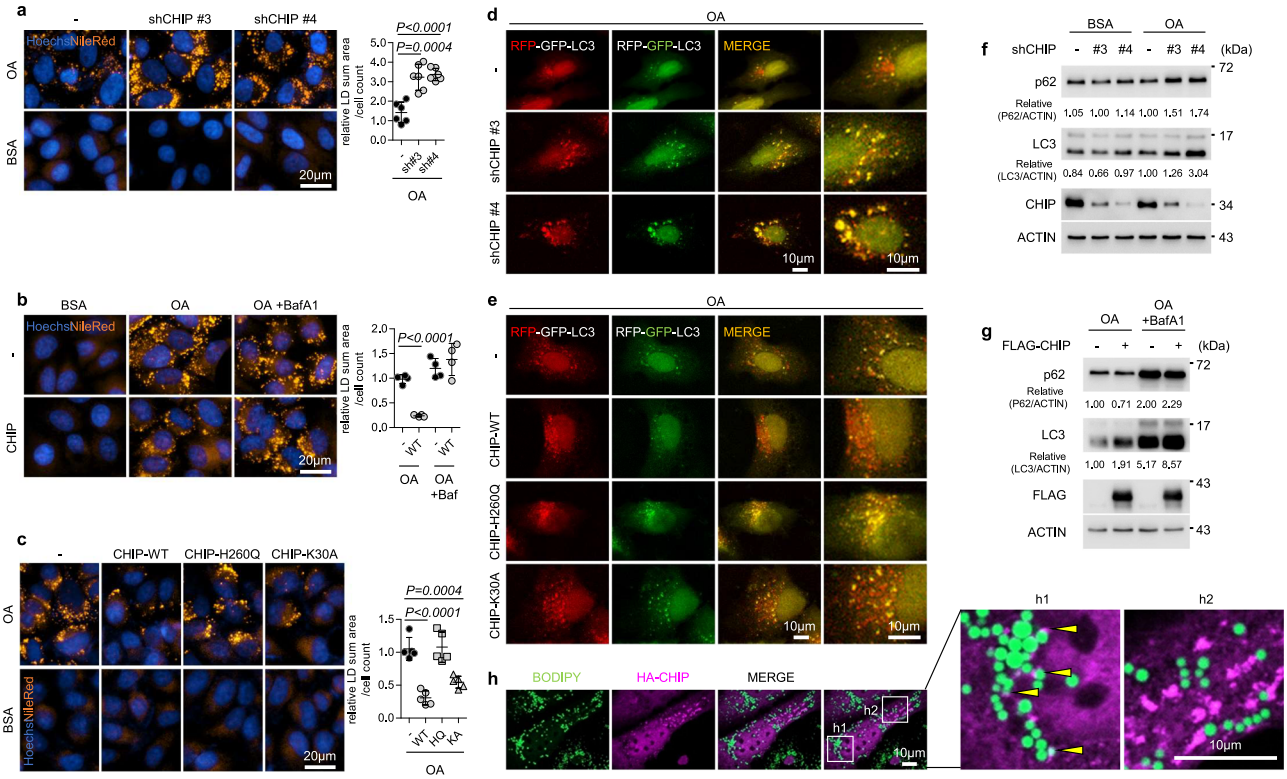

Fig. 2 | CHIP promotes the lipophagy pathway by facilitating autolysosome formation. Representative images demonstrate lipid staining with Nile red (orange) and Hoechst staining of DNA (blue). The image dataset contains at least 4 randomly chosen fluorescence microscopy images. **a** HepG2 cells with CHIP knockdown, stable overexpression of (**b**) CHIP-WT, (**c**) CHIP-WT, CHIP-H260Q, or CHIP K30A were treated with OA overnight. Representative images with autophagosome (yellow puncta) and autolysosome (red puncta) are shown. **d** HepG2 cells with CHIP knockdown or (**e**) stable overexpression of CHIP-WT, CHIP-H260Q, or CHIP-K30A were transfected with RFP-GFP-LC3 and treated with OA overnight. **f** HepG2 cells with CHIP knockdown or (**g**) FLAG-CHIP overexpression were treated with or without OA and BafA1, followed by western blot analysis. **h** Confocal microscopy immunofluorescence of HA-CHIP (magenta) and lipid staining with BODIPY 493/503 (green) showed the colocalization of CHIP and lipid droplets (h1) and the decreased level of lipid droplets around the region of CHIP with high expression (h2). Data are presented as individual data points, mean ± SD is assessed by unpaired two-tailed *t*-test. LD lipid droplet, BSA bovine serum albumin, OA oleic acid, BafA1 bafilomycin A1.

not significantly associated with liver-related metabolic pathways (Supplementary Fig. 3q-r).

As H-KO mice fed NCD exhibited no phenotypes, H-KO mice were subjected to 20 weeks of metabolic stress with an HFD (Fig. 3a). Although the mice exhibited no differences in weight gain, food intake, or fat accumulation in SubQ, Epi, and BAT (Supplementary Fig. 4a-e), H-KO mice exhibited hepatomegaly and a higher percentage ratio of liver weight/body weight (LW/BW; Fig. 3b). In addition, H-KO mouse livers exhibited increased P62 and LC3 accumulation compared to those of WT mice, indicating the suppression of late-stage autophagy (Fig. 3c and Supplementary Fig. 4f). The H-KO mice exhibited a greater increase in steatosis and macrophage infiltration, corroborating these findings (Fig. 3d–f). HFD nutrition for 20 weeks has been reported to induce uncomplicated steatosis without fibrosis in mice[41]. The H-KO mice exhibited severe liver fibrosis (Fig. 3g) and elevated hepatic TG and TC levels (Fig. 3h). Serum levels of TG, TC, VLDL, FFA, HDL, and LDL were reduced in H-KO mice (Supplementary Fig. 4g-h), indicating the suppression of autophagy-associated VLDL release, as previously described[42]. Serum β-hydroxybutyrate (β-HB) levels were also decreased in H-KO mice, suggesting that autophagy was impaired under CHIP depletion[43] (Supplementary Fig. 4i). Serum ALT and AST levels were elevated in H-KO mice, suggesting enhanced liver damage due to induction of metabolic stress with an HFD (Fig. 3i). The transcript levels of genes associated with inflammation and fibrosis were upregulated in H-KO mice (Supplementary Fig. 4j, k), whereas transcript levels of lipogenesis-, lipolysis-, and autophagy-related genes (Supplementary Fig. 4l-n) showed no significant differences, suggesting that CHIP may regulate lipophagy at the post-translational level.

As NAFLD is strongly associated with T2DM[44], we evaluated the effects of CHIP on glucose and insulin tolerance. H-KO mice displayed decreased tolerance to glucose or insulin administration (Fig. 3j, k). Lower levels of phosphorylated AKT were observed in H-KO mice than in WT mice, indicating suppression of the insulin-mediated signaling pathway (Fig. 3l). In support of these findings, the serum insulin levels of H-KO mice increased, indicating hyperinsulinemia (Supplementary Fig. 4o). Overall, the autophagy pathway was inhibited in H-KO mice, which may have exacerbated steatosis, fibrosis, inflammation, and metabolic syndromes, such as T2DM, when fed an HFD.

Impaired hepatic lipophagy in HFD-fed H-KO mouse liver induces NASH-like phenotypes via activating aHSCs, M1 Kupffer cells, and pro-inflammatory T cell activation in a protein-dependent manner

Single-nucleus RNAseq (snRNAseq) analyses of three samples each of HFD-fed WT and H-KO mouse livers were performed to analyze the hepatocyte-specific regulatory role of CHIP (Fig. 4a). Thirty-three clusters were identified among 71,058 cells, which were categorized into 11 cell types (Fig. 4b, c and Supplementary Figs. 5, 6). The GSEA data of the top ten regulated pathways in hepatocytes based on snRNAseq indicate that biosynthetic processes were majorly upregulated in H-KO hepatocytes (Fig. 4d). However, there were no significant differences in the pathways such as glycolysis,

https://doi.org/10.1038/s41467-024-53002-0

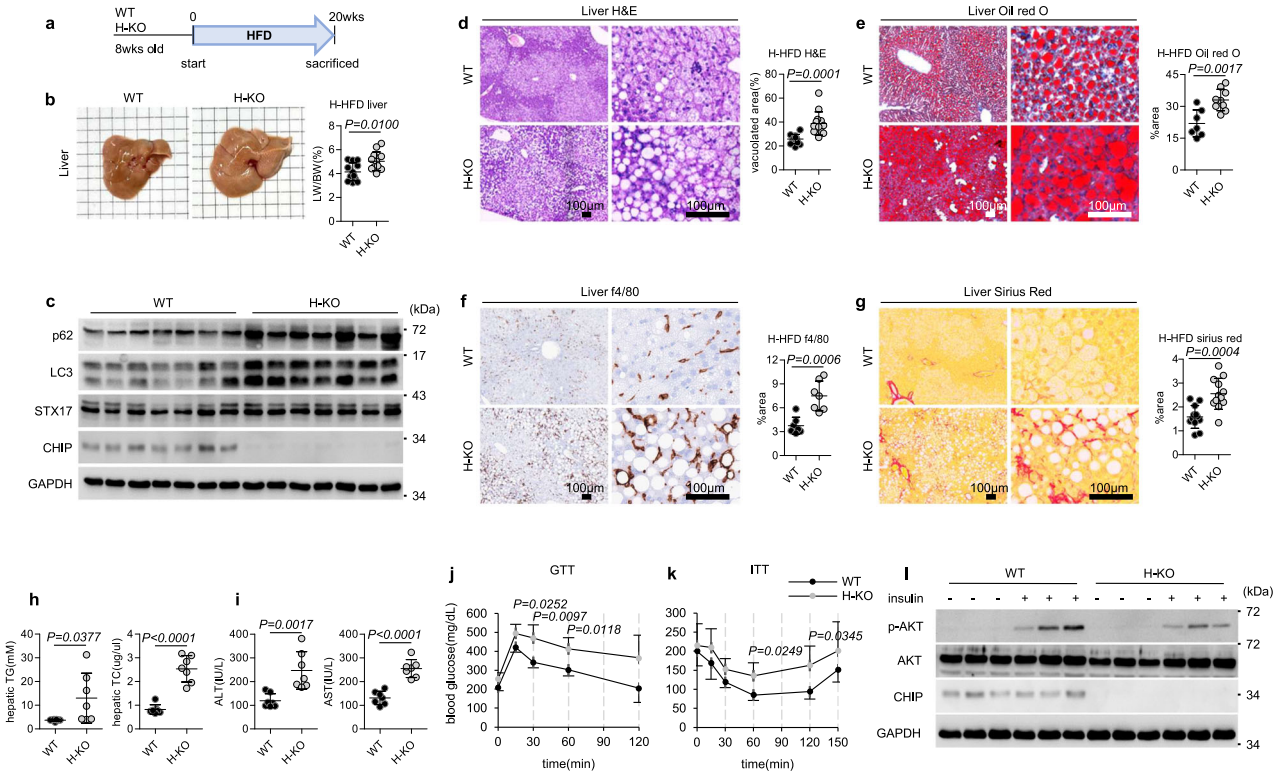

Fig. 3 | HFD exacerbates liver steatosis, inflammation, fibrosis, and metabolic syndromes in H-KO mice. a Eight-week-old WT and H-KO mice individually housed were fed a HFD for 20 weeks. **b** Representative livers of mice fed a HFD (left), and the calculated percentage of liver weight/body weight ratio (right). Grid cubes are 5 mm*5 mm. **c** Representative western blot images exhibiting P62, LC3, and STX17 expression in the liver samples of HFD-fed mice. **d**–**g** Representative images of liver samples stained with H&E (n = 13), Oil red O (WT, n = 7; H-KO, n = 9), f4/80 immunohistochemistry (n = 7), and Sirius red (n = 12). **h**–**i** Hepatic TG and TC levels, and serum ALT and AST levels in mice fed an HFD (n = 7). **j** Glucose tolerance tests (n = 5) and **k** insulin tolerance tests (n = 5) were conducted. **l** Representative western blot images demonstrating the insulin-stimulated phosphorylation of AKT in livers. Mice were injected with either PBS (−) or insulin (+). The error bars in (**j**) and (**k**) indicate SD. Data are presented as individual data points, mean ± SD is assessed by unpaired two-tailed *t*-test.

gluconeogenesis, β-oxidation, fatty acid synthesis, lipogenesis, mitochondrial biogenesis, cell growth, and autophagy between the two groups (Fig. 4e). This may be because both WT and H-KO mice were fed with HFD, which led to various metabolic dysfunctional syndromes in both mice.

As hepatic stellate cells can induce liver fibrosis[45], we identified 11 clusters of hepatic stellate cells (HSCs) which were classified into quiescent HSCs (qHSCs) and activated HSCs (aHSCs) (Fig. 4f and Supplementary Fig. 7). While a slight increase in the aHSC proportion was observed in H-KO mice samples compared with WT, H-KO samples significantly exhibited more up-regulated fibrosis- and activation-related gene expressions in aHSC clusters (*agtr1a, mertk, aldh1a1, klf9, papss2*) and down regulated gene expressions in qHSC clusters (*tgfbi, smad6, cdk8, itih3*), indicating increased fibrosis (Fig. 4f, g). Furthermore, the DEGs of Kupffer cells exhibited increased M1 macrophage polarization and suppressed M2 macrophage polarization related gene expressions in H-KO samples (Fig. 4h). DEGs of T cells exhibited increased pro-inflammatory T cell activation, decreased resident memory T cells, and anti-pro-inflammatory T cell activation-related gene expressions in H-KO samples (Fig. 4i). Thus, CHIP knockout in hepatocytes may make the cells more susceptible to lipotoxicity leading to more hepatocyte cell death and liver scarring. Moreover, the lack of much difference in transcriptional patterns in hepatocytes between WT and H-KO under HFD seems to indicate that lipid accumulation due to the blocking of the autophagosome-lysosome fusion process in HFD-fed H-KO mice liver is more regulated through a protein-dependent manner than at transcriptional levels.

H-KO mice develop severe NASH under an HFHFD

To further investigate the effects of CHIP on NAFLD progression, WT and H-KO mice were fed an HFHFD for 24 weeks (Fig. 5a). Weight gain, food intake, fructose intake, or the phenotypes of SubQ, Epi, and BAT showed no differences (Supplementary Fig. 8a-f). The H-KO mice displayed hepatomegaly and a higher percentage of LW/BW ratio (Fig. 5b). In addition, p62 and LC3 levels were elevated in H-KO mouse liver samples, indicating that autophagy progression was impeded (Fig. 5c, d). Histochemical analyses revealed more severe forms of steatosis, macrophage infiltration, and fibrosis in H-KO mouse livers (Fig. 5e-h), and elevated hepatic TG and TC levels (Fig. 5i), which resulted in increased serum ALT and AST levels compared to those in WT mice (Fig. 5j). H-KO mice exhibited decreased serum TG, TC, VLDL, FFA, HDL, LDL, and β-HB levels under HFHFD, supporting the role of CHIP in the inhibition of the autophagy pathway and β-oxidation (Supplementary Fig. 8g-i). As expected, the transcript levels of genes related to inflammation and fibrosis were also elevated in H-KO mouse liver samples (Fig. 5k, l). Overall, these findings suggest that the absence of CHIP in mouse hepatocytes may suppress the autophagy pathway (lipophagy), thereby worsening liver injury under an HFHFD and resulting in NASH phenotypes of increased severity.

CHIP promotes SNARE complex formation, which is necessary for autophagosome and lysosome fusion

In vitro and in vivo data suggested that CHIP plays a role in the autophagosome-lysosome fusion process. Since the STX17-SNAP29-VAMP8 SNARE complex plays essential roles in autophagosome-lysosome fusion, the correlation between SNARE complexes and CHIP

https://doi.org/10.1038/s41467-024-53002-0

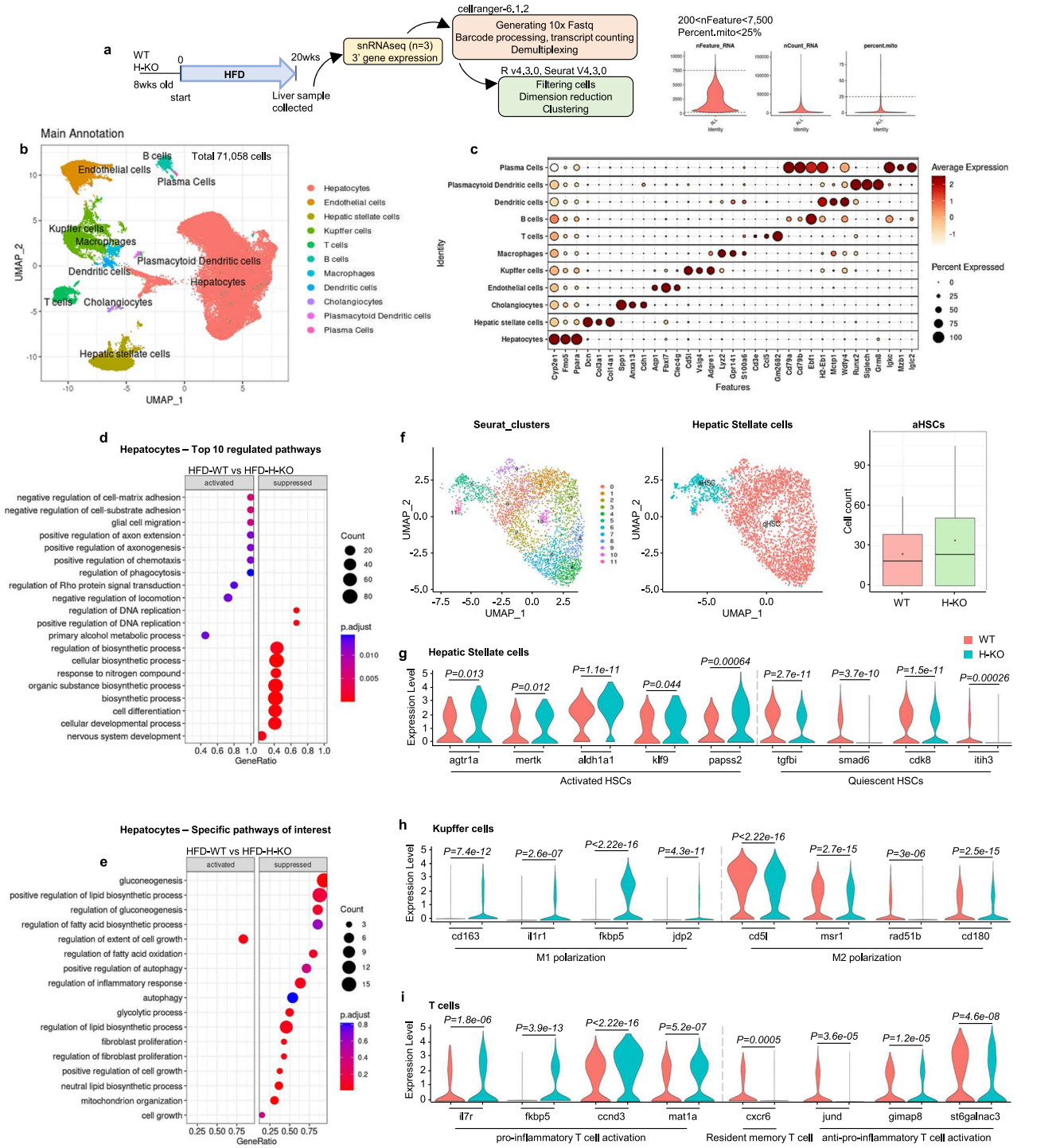

Fig. 4 | Impaired hepatic lipophagy in HFD-fed H-KO mouse liver induces NASH-like phenotypes via activating aHSCs, M1 Kupffer cells, and pro-inflammatory T cell activation in a protein-dependent manner. a Schematic representation of snRNAseq analysis of HFD-fed WT and H-KO mouse livers (n = 3). **b** Uniform manifold approximation and projection (UMAP) visualize clustering of liver single-nucleus transcriptomes (Total 71,058 cells), and the color represents annotations of different cell types. Thirty-three clusters were identified into 11 cell types. **c** Dot plot displaying the expression of cell-type-specific marker genes used to identify liver cell populations. **d** GSEA data of top 10 regulated pathways in hepatocytes. **e** GSEA data of pathways related to metabolism, inflammation, and fibrosis in hepatocytes. **f** UMAP visualizes subclustering of HSCs from 11 clusters to qHSCs and aHSCs and the color represents annotation of different cell types. Box and whisker plot indicates the proportion of qHSCs and aHSCs in WT and H-KO samples (n = 3). The top end of vertical line represents the maximum value, the horizontal lines represent third quartile, median, and first quartile from the top to bottom, and the dot represents the average. **g**–**i** Violin plots of representative DEGs in aHSCs, qHSCs, Kupffer cells, and T cells, respectively. Statistical analyses of RNAseq results were performed using the Wilcox test in R version 4.3.0. HSCs hepatic stellate cells, qHSCs quiescent HSCs, aHSCs activated HSCs.

https://doi.org/10.1038/s41467-024-53002-0

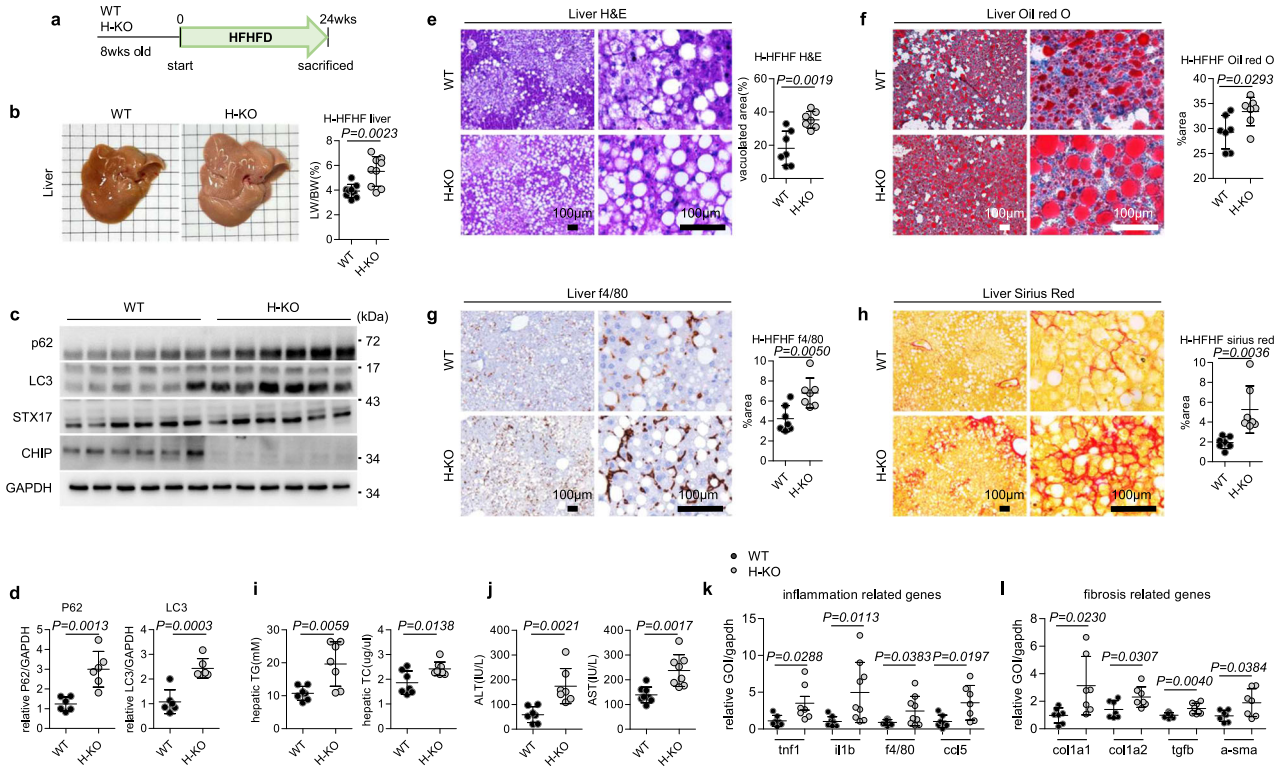

Fig. 5 | H-KO mice develop severe NASH under a HFHFD. a Eight-week-old WT and H-KO mice individually housed were fed a HFHFD for 24 weeks. **b** Representative livers of mice fed a HFHFD (left), and the calculated percentage of liver weight/body weight ratio (right) (n = 9). Grid cubes are 5 mm*5 mm. **c**, **d** Representative western blot images and quantitation graph exhibiting P62, LC3, and STX17 expression in the liver samples of HFHFD-fed mice (n = 6). **e**–**h** Representative images of liver samples (n = 7) stained with H&E, Oil red O, f4/80 immunohistochemistry, and Sirius red. **i**, **j** Hepatic TG (n = 7) and TC (WT, n = 7; H-KO, n = 8) levels, and serum ALT (n = 7) and AST (n = 8) levels in mice fed a HFHFD. **k**, **l** qRT-PCR was used to quantify the relative transcript levels of inflammation and fibrosis genes in mouse liver samples (n = 7–9). Data are presented as individual data points, mean ± SD is assessed by unpaired two-tailed *t*-test. GOI, gene of interest.

was further analyzed. STX17 levels were decreased in NASH patients compared to controls (Fig. 6a and Supplementary Fig. 9a). Similarly, HFD- and HFHFD-treated mice exhibited reduced hepatic STX17 levels compared to mice with NCD (Fig. 6b, c). STX17 and CHIP expression levels were positively correlated in both normal and NASH patients (Supplementary Fig. 9b), indicating that STX17 and CHIP are plausible biomarkers for NASH. The decreased expression of CHIP and STX17 under NAFLD progression led to decreased colocalization between CHIP and STX17 (Supplementary Fig. 9c), which led to decreased SNARE complex assembly (Supplementary Fig. 10a, b). To further investigate the interaction between CHIP and SNARE complexes, various biochemical analyses were performed. Because of the absence of effective human antibodies for detecting endogenous VAMP8, we overexpressed HA-VAMP8 or FLAG-VAMP8 in cells to facilitate its detection. CHIP was detected along with STX17, SNAP29, and HA-VAMP8 when anti-STX17 antibodies were used for immunoprecipitation (Fig. 6d). Particularly, STX17 and VAMP8 interacted with CHIP via overexpression immunoprecipitation assay (Fig. 6e). In an OA-rich environment, the interaction between the SNARE complex and CHIP increased, indicating that CHIP participated in the autophagosome-lysosome fusion pathway via regulating SNARE complex formation (Fig. 6f). Supporting these findings, CHIP reduction in HepG2 and primary hepatocytes decreased the SNARE complex assembly, as detected by SNAP29 and VAMP8 binding to STX17 (Fig. 6g, h). The SNARE complex formation increased only when functional CHIP WT was overexpressed, indicating that CHIP-mediated ubiquitination may be crucial for SNARE complex formation (Fig. 6i). Additional experiments confirmed the co-localization of CHIP and STX17 in an OA-rich environment endogenously and exogenously (Fig. 6j, k). Using immunofluorescence, the ability of CHIP to facilitate SNARE complex formation was evaluated. Under OA treatment, CHIP depletion decreased STX17 and VAMP8 co-localization, whereas CHIP overexpression increased these processes (Fig. 6l, m). This effect was substantially inhibited via overexpression of H260Q (Fig. 6m). Moreover, the SNARE complex formation decreased in liver samples of H-KO mice fed HFD and HFHFD (Supplementary Fig. 10c). Overall, CHIP modulates SNARE complex formation via increasing SNAP29 and VAMP8 recruitment to STX17, presumably through CHIP-mediated ubiquitination.

CHIP-mediated K63- and K27-linked ubiquitination of the STX17 K198 residue accelerates SNARE complex formation

Since STX17 and VAMP8, but not SNAP29, could interact with CHIP (Fig. 6b), we investigated potential targets of CHIP for ubiquitination. Analyses of endogenous STX17 and VAMP8 ubiquitination in an OA-rich environment revealed that only STX17 was ubiquitinated (Fig. 7a and Supplementary Fig. 12a, b). We did not observe ubiquitination of VAMP8 or other autophagy factors by CHIP (Supplementary Figs. 11 and 12c). However, ubiquitinated STX17 levels were significantly reduced in the absence of CHIP (Fig. 7b and Supplementary Fig. 12d), whereas they increased under CHIP or K30A mutant overexpression (Fig. 7c and Supplementary Fig. 12e), indicating that CHIP was responsible for the OA-induced ubiquitination of STX17. Further, the ubiquitination of STX17 in liver samples was decreased in HFD-fed H-KO mice when compared with WT mice (Supplementary Fig. 12f).

Next, we analyzed the specific ubiquitination targets of STX17 using CHIP. STX17 deletion mutants including H (1-123), ΔH (124-303), ΔHT (124-227), and T (228-303) were generated based on its helix a, b,

https://doi.org/10.1038/s41467-024-53002-0

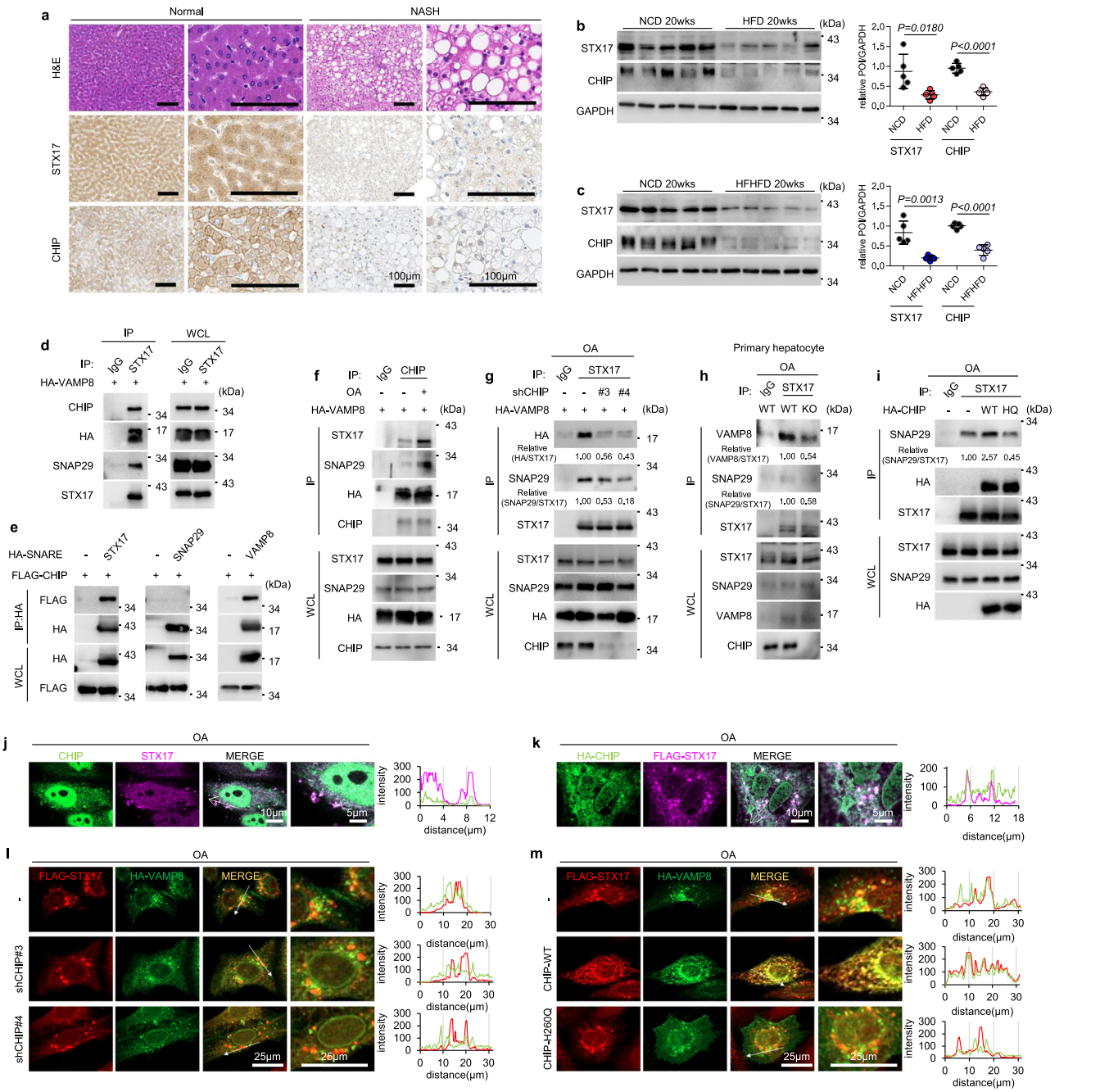

Fig. 6 | CHIP promotes SNARE complex formation, which is necessary for autophagosome and lysosome fusion. a Representative immunohistochemical staining images for CHIP and STX17 in formalin-fixed paraffin-embedded (FFPE) liver tissues. H&E staining of FFPE human liver samples diagnosed as normal and NASH are shown at top of the image. Scale bar shown is 100 μm. **b**, **c** Mice were fed a NCD, HFD, or HFHFD for 20 weeks (n = 5). Western blotting and quantification of the liver samples. **d** Lysates of HepG2 cells transfected with the plasmid expressing HA-VAMP8 were immunoprecipitated using anti-STX17 antibodies, followed by western blotting. **e** The plasmid expressing FLAG-CHIP was co-transfected with the plasmid expressing HA-STX17, HA-SNAP29, or HA-VAMP8 in 293FT cells. The lysates were immunoprecipitated using anti-HA antibodies, followed by western blotting. **f** HepG2 cells expressing HA-VAMP were treated with OA. The lysates were immunoprecipitated with anti-CHIP antibodies, followed by western blotting. Lysates from each cell type treated with OA overnight were immunoprecipitated with anti-STX17 antibodies, followed by western blotting. **g** HepG2 cells stably transfected with plasmids #3 or #4 expressing CHIP-shRNAs. **h** Primary hepatocytes isolated from WT and H-KO mice. **i** HepG2 cells transfected with plasmids overexpressing HA-CHIP-WT, HA-CHIP-H260Q, or HA-CHIP-K30A. Immunofluorescence analyses of HepG2 cells using confocal microscopy was conducted as follows: **j** HepG2 cells; **k** HepG2 cells were transfected with the plasmid expressing HA-CHIP and FLAG-STX17; **l** CHIP was knocked down in HepG2 cells, followed by transfection with plasmids expressing FLAG-STX17 and HA-VAMP. **m** HepG2 cells stably overexpressing CHIP-WT, CHIP-H260Q, or CHIP-K30A were transfected with plasmids overexpressing FLAG-STX17 and HA-VAMP8. HepG2 cells overexpressing indicated plasmids were treated with OA overnight, followed by immunofluorescent analysis employing anti-CHIP, anti-STX17, anti-HA, and anti-FLAG antibodies. The graphs indicate fluorescence intensities (white arrow). Data are presented as individual data points, mean ± SD is assessed by unpaired two-tailed *t*-test.

https://doi.org/10.1038/s41467-024-53002-0

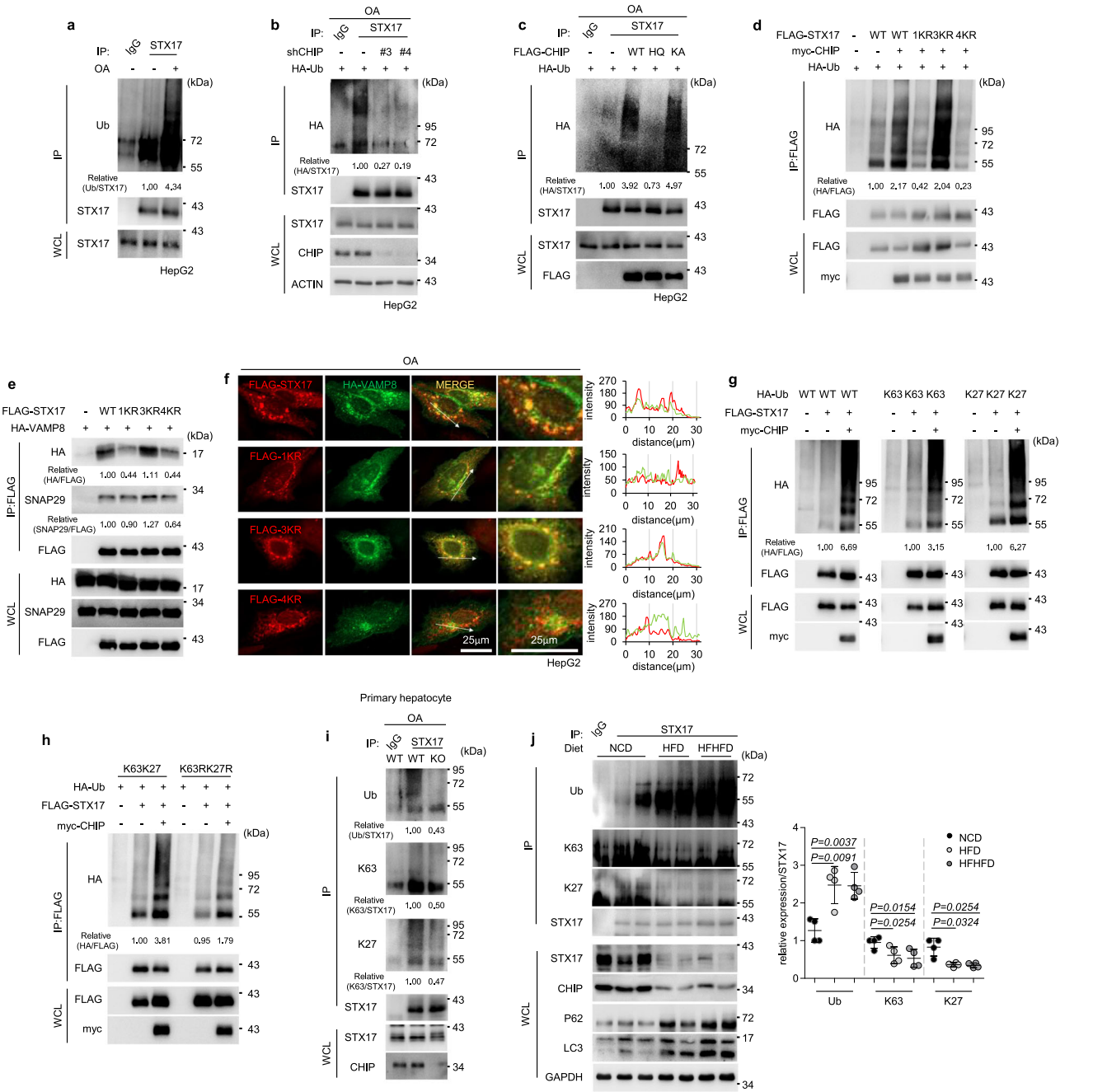

Fig. 7 | CHIP-mediated K63- and K27-linked ubiquitination of the STX17 K198 residue accelerates SNARE complex formation. a Lysates of HepG2 cells treated with or without OA were immunoprecipitated using anti-STX17 antibodies, followed by western blotting. **b**, **c** HepG2 cells stably transfected with HA-Ub, and plasmid #3 or #4 expressing CHIP-shRNA, or plasmids overexpressing FLAG-CHIP-WT, FLAG-CHIP-HQ, or FLAG-CHIP-KA, as indicated, were treated with OA overnight. Lysates were immunoprecipitated using anti-STX17 antibodies, followed by western blotting. **d**, **e** 293FT cells were transfected with plasmids expressing FLAG-STX17-WT, FLAG-STX17-1KR, FLAG-STX17-3KR, FLAG-STX17-4KR, myc-CHIP, HA-Ub, or HA-VAMP8, as indicated. Cell lysates were immunoprecipitated with anti-FLAG antibodies, followed by western blotting. **f** Immunofluorescence analysis of HepG2 cells was conducted by confocal microscopy, as follows. Cells were treated with OA overnight and transfected with plasmids expressing FLAG-STX17-WT, FLAG-STX17-1KR, FLAG-STX17-3KR, FLAG-STX17-4KR, and HA-VAMP8, as indicated, followed by immunofluorescence analysis using anti-FLAG and anti-HA antibodies. Graphs indicate the fluorescence intensity (white arrow). **g**, **h** 293FT cells were transfected with plasmids expressing HA-Ub-WT, HA-Ub-K63, HA-Ub-K27, HA-Ub-K63K27, HA-UbK63RK27R, FLAG-STX17, or myc-CHIP, as indicated. Cell lysates were immunoprecipitated with anti-FLAG antibodies, followed by western blotting. Lysates of (**i**) primary hepatocytes isolated from WT and H-KO mice, and (**j**) NCD-, HFD-, and HFHFD-fed mouse liver samples immunoprecipitated using anti-STX17 antibodies, followed by western blotting (n = 4). Data are presented as individual data points, mean ± SD is assessed by paired two-tailed *t*-test.

and c domain (Habc), Qa-SNARE, and two transmembrane domains (T)[46] (Supplementary Fig. 12g). Only ΔH and ΔHT mutants interacted with CHIP and were ubiquitinated when CHIP-mediated binding and ubiquitination of each domain were evaluated (Supplementary Fig. 12h, i). Hypothesizing that ΔHT, including the Qa-SNARE domain, may contain ubiquitination sites targeted by CHIP, we generated three types of point mutants via replacing the lysine (K) sites at 198, 218, 222, and 225 with arginine (R). The mutants K198R (1KR), K218RK222RK225R (3KR), and K198RK218RK222RK225R (4KR) were generated and evaluated for susceptibility to ubiquitination by CHIP

(Supplementary Fig. 12g). Both 1KR and 4KR mutants exhibited resistance to CHIP-mediated ubiquitination (Fig. 7d and Supplementary Fig. 12j). Furthermore, the ability of the 1KR and 4KR mutants to interact or co-localize with VAMP8 was significantly diminished (Fig. 7e, f). As CHIP had no effect on the protein expression levels of STX17, we hypothesized that CHIP-mediated ubiquitination is associated with the ubiquitin-mediated signaling pathway. Using K6, 11, 27, 29, 33, 48, or 63-only ubiquitin to test for CHIP-dependent ubiquitination[47], we observed that CHIP promoted K63- or K27-only-linked ubiquitination of STX17 (Fig. 7g and Supplementary Fig. 12k-l). Introduction of a single arginine (R) mutation at either the K63 or K27 site did not prevent the STX17 ubiquitination by CHIP (Supplementary Fig. 12m); however, the introduction of a double mutant ubiquitin, K63RK27R, significantly reduced the CHIP-mediated ubiquitination of STX17, indicating that both the K63 and K27 sites were necessary for the ubiquitination process (Fig. 7h and Supplementary Fig. 12n). Furthermore, the absence of STX17 ubiquitination by CHIP in the 1KR mutant was observed when K63- and K27-only ubiquitin was expressed (Supplementary Fig. 12o). To better evaluate physiological CHIP-mediated STX17 ubiquitination, we performed experiments using primary hepatocytes and liver samples. H-KO primary hepatocytes treated with OA exhibited decreased net, K63-, and K27-linked STX17 ubiquitination (Fig. 7i and Supplementary Fig. 12p). While previous reports described upregulated net ubiquitination of STX17 in the liver during NAFLD progression[15], K63- and K27-linked ubiquitination was decreased, correlating with decreased CHIP levels (Figs. 7j, and 1c–f). In summary, the findings of this study demonstrate that CHIP-mediated ubiquitination targets the STX17 protein at the K198 residue, utilizing both K63- and K27-linked ubiquitin chains. The ubiquitination processes at K198 of STX17 appear to be essential, as the STX17 mutant 1KR exhibited a significant decrease in its capacity to form STX17-SNAP29-VAMP8 complexes.

STX17 1KR mutant is defective in CHIP-mediated ubiquitination, preventing lipophagy under an HFD

As the 1KR and 4KR mutants were no longer targeted by CHIP for ubiquitination with a significant reduction in SNARE complex formation, we subsequently evaluated the ability of STX17 to regulate lipophagy. STX17-depleted HepG2 cells exhibited increased P62 and LC3 levels, and the number of yellow puncta increased when RFP-GFP-LC3 was expressed, indicating the inhibition of autophagosome-lysosome fusion (Fig. 8a and Supplementary Fig. 13a-b). Lipid droplet accumulation also increased under STX17 knockdown (Supplementary Fig. 13c). When STX17 WT and 3KR were overexpressed in cells, RFP-GFP-LC3 expression displayed red puncta (Fig. 8b and Supplementary Fig. 13d-e) and decreased lipid accumulation occurred (Supplementary Fig. 13f), indicating lipophagy activation. Thereby, we confirmed the association between CHIP and STX17 signaling axes. Reduced STX17 levels prevented lipid degradation in CHIP-overexpressing cells (Fig. 8c and Supplementary Fig. 13 g). Consistent with this finding, when CHIP was depleted in cells overexpressing STX17, comparable effects were observed (Fig. 8d and Supplementary Fig. 13h). These data indicated that CHIP and STX17 may be on the same signaling axis.

To further confirm the effects of STX17 and its K198 (K197 in mice) residue in vivo, 8-week-old mice were fed an HFD for 10 weeks, followed by intravenous injection of the control (CON), HA-mSTX17-WT (mSTX17), or HA-mSTX17-1KR (m1KR) plasmids on days 4 and 1 prior to sacrifice (Supplementary Fig. 14a). Mice exhibited a modest decrease in body weight and food intake due to the potential effects of the delivery reagents (Supplementary Fig. 14b, c); however, while the plasmids were effectively delivered to each group (Supplementary Fig. 14d), no other significant physiological differences were observed in SubQ, Epi, and BAT among the tested mice (Supplementary Fig. 14e–g). The percentage of LW/BW ratio in the mSTX17 mice was lower than that in the CON mice (Fig. 8e). While histological analyses revealed no significant differences in macrophage infiltration and fibrosis with the HFD (Supplementary Fig. 14h, i), hepatic steatosis was reduced in the livers of mSTX17 mice compared to that in CON or m1KR mice (Fig. 8f, g). Hepatic TG and TC levels were lower in the mSTX17 mice than in the CON and m1KR mice (Fig. 8h). The mSTX17 mice also exhibited decreased serum AST levels (Supplementary Fig. 13i). Diminished transcript levels of genes associated with inflammation and fibrosis were also observed in the livers of mSTX17 mice and not in the livers of CON or m1KR mice (Supplementary Fig. 14j, k). Further, electron microscopy analysis demonstrated that mSTX17 overexpression in the liver significantly increased the formation of autolysosomes compared to that in CON or m1KR mice. As expected, m1KR overexpression enhanced autophagosome accumulation in the liver, possibly due to autophagy inhibition (Fig. 8i). Notably, enlarged lipid-containing autophagosomes were observed in m1KR-overexpressing mouse livers, supporting that autophagy, specifically lipophagy, might be inhibited due to blockage of autophagosome and lysosome fusion (Fig. 8j). This was further confirmed using western blot analysis, which showed that autophagy was activated in the mouse livers expressing mSTX17, as indicated by decreased P62 and increased LC3-II levels. In contrast, mouse livers expressing m1KR displayed retarded autophagy, as indicated by increased P62 and LC3 levels compared to that in livers expressing CON or mSTX17 (Supplementary Fig. 14l). Supporting these data, serum TG and VLDL levels were lower in mSTX17 and m1KR mice than in CON mice (Supplementary Fig. 13j-k). Furthermore, net, K63-, and K27-linked STX17 ubiquitination was significantly decreased in m1KR-overexpressing mouse livers when compared to mSTX17 mice (Fig. 8k). SNARE complex formation was increased in mSTX17 mouse liver samples when compared to CON and m1KR (Fig. 8l). These results suggest that CHIP-mediated STX17 ubiquitination at K198 (K197 in mice) may be important for STX17-SNAP29-VAMP8 complex formation for autophagosome-lysosome fusion under physiological conditions.

AAV8-mediated CHIP overexpression in the liver inhibits NAFLD progression in response to HFD or HFHFD

As the depletion of CHIP in the liver appears to accelerate NAFLD progression, the AAV8 system, which primarily infects the liver, was used to investigate the therapeutic effects of CHIP overexpression in the liver. We first confirmed that CHIP was overexpressed in the liver via western blotting of multiple tissue samples (Supplementary Fig. 15a). To induce metabolic syndromes, eight-week-old mice were fed an HFD for eight weeks, followed by an intravenous injection of AAV8-GFP control (CON) or AAV8-CHIP-GFP (OE) with an additional eight weeks of feeding the HFD (Supplementary Fig. 15b). The mice showed no differences in weight gain, food intake, or physiological alterations in adipose tissues (Supplementary Fig. 16a-e); however, OE mice had a smaller liver with a healthier morphology and a lower percentage of LW/BW ratio (Fig. 9a). CHIP overexpression decreased the P62 levels and increased the LC3-II levels, indicating a more active autophagy process in the livers of OE mice (Supplementary Fig. 16f). Histochemical analyses of the livers of the OE mice revealed diminished steatosis and macrophage infiltration, but no significant differences in fibrosis (Fig. 8b-d and Supplementary Fig. 15c-e). In contrast, the transcript levels of genes related to inflammation and fibrosis decreased in the livers of OE mice (Supplementary Fig. 16g-h), indicating that CHIP overexpression has beneficial effects on fibrosis and inflammation under persistent metabolic syndrome induction. Hepatic and serum analyses revealed decreased TG, TC, ALT, AST, VLDL, FFA, HDL, LDL, and β-HB concentrations (Fig. 9e-f and Supplementary Fig. 16i-k). We further investigated the effects of CHIP overexpression on the HFD-related metabolic syndromes. As anticipated, OE mice exhibited decreased hyperinsulinemia (Supplementary Fig. 16l), improved glucose tolerance and insulin sensitivity (Fig. 9g, h), followed by

https://doi.org/10.1038/s41467-024-53002-0

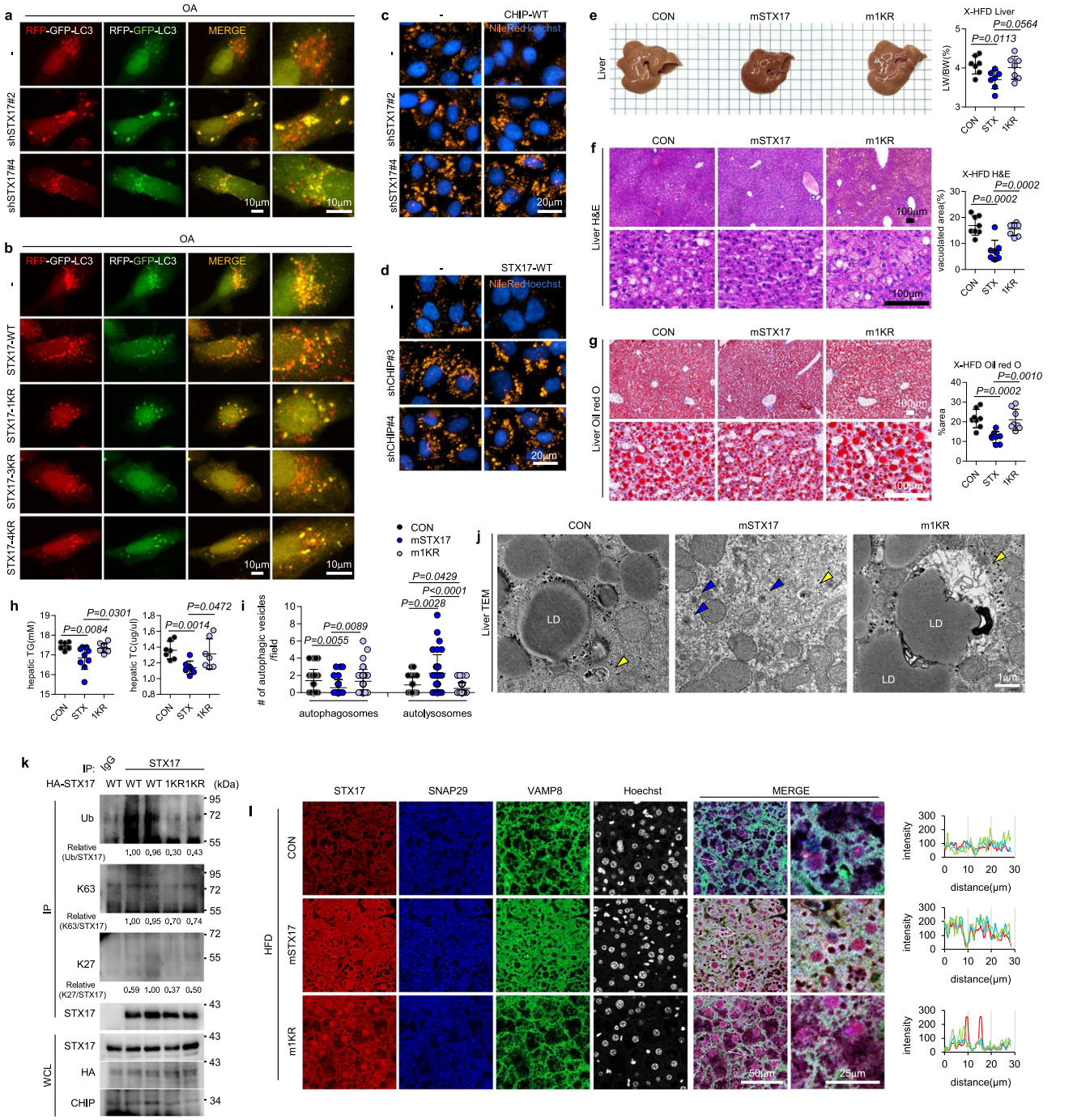

Fig. 8 | STX17 1KR mutant is defective in CHIP-mediated ubiquitination, preventing lipophagy under an HFD. Representative images with autophagosome (yellow puncta) and autolysosome (red puncta). **a** HepG2 cells with STX17 knockdown or (**b**) stable overexpression of STX17-WT, STX17-1KR, STX17-3KR or STX17-4KR were transfected with RFP-GFP-LC3 and treated with OA overnight. Representative images demonstrating lipid staining with Nile red (orange) and Hoechst staining of DNA (blue). **c** HepG2 cells stably overexpressing CHIP-WT were co-transfected with plasmids #2 or #4 expressing STX17-shRNAs, and (**d**) HepG2 cells overexpressing STX17-WT were co-transfected with plasmids #3 or #4 expressing CHIP-shRNAs. Both cell lines were treated with OA overnight. Eight-week-old mice were individually housed for 10 weeks with a HFD and intravenously injected with the plasmids expressing control (CON), HA-mSTX17-WT (mSTX), or HA-mSTX17-1KR (m1KR) on days 4 and 1 prior to sacrifice. **e** Representative livers of mice fed a HFD (left) and the calculated percentage of liver weight/body weight ratio (right) (n = 7). Grid cubes are 5 mm*5 mm. **f**, **g** Representative images of liver samples stained with H&E or Oil red O (n = 8). **h** Hepatic TG (n = 9) and TC (n = 7) levels in mice fed an HFD. **i** Calculated number of autophagic vesicles per field (n = 4). **j** Representative TEM images (n = 4). Autophagosomes (yellow arrows) and autolysosomes (blue arrows) are indicated in the images. **k** Lysates of mSTX17 and m1KR liver samples were immunoprecipitated with anti-STX17 antibodies, followed by western blotting. **l** Immunofluorescence analyses of CON, mSTX17, and m1KR mouse liver samples using confocal microscopy were conducted using anti-STX17, anti-SNAP29, and anti-VAMP8 antibodies. Graphs indicate fluorescence intensities (white arrow). Data are presented as individual data points, mean ± SD is assessed by unpaired two-tailed *t*-test. LD lipid droplet.

https://doi.org/10.1038/s41467-024-53002-0

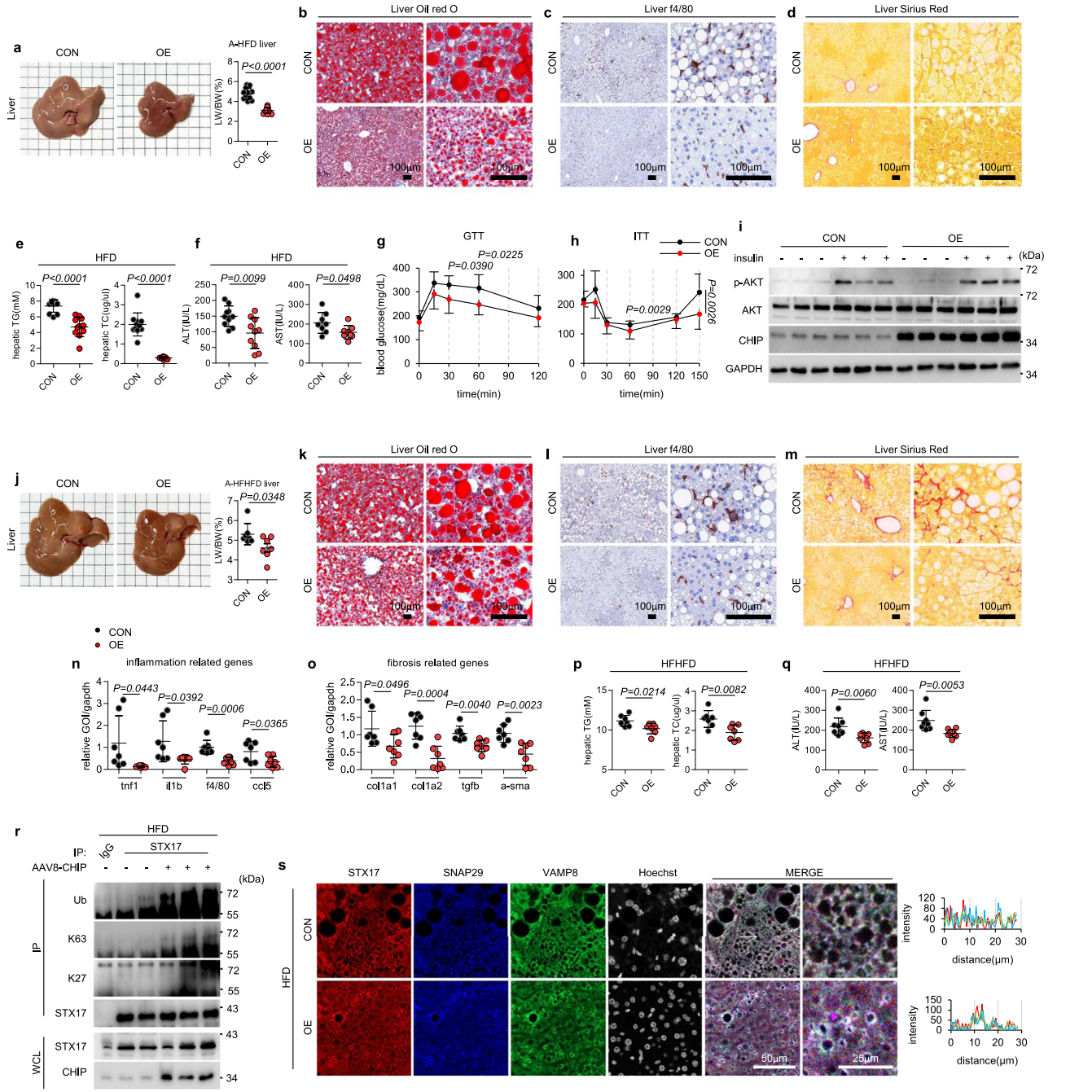

Fig. 9 | AAV8-mediated CHIP overexpression in the liver inhibits NAFLD progression in response to HFD or HFHFD. a–**i**; **r**, **s** Eight-week-old mice were individually housed for 16 weeks with a HFD and intravenously injected with AAV8-GFP or AAV8-CHIP-GFP 8 weeks prior to sacrifice. **a** Representative livers of mice fed a HFD (left) and the calculated percentage of liver weight/body weight ratio (right) (n = 12). Grid cubes are 5 mm*5 mm. **b**–**d** Representative images of liver samples stained with Oil red O, f4/80 immunohistochemistry, and Sirius red. **e**, **f** Hepatic TG (n = 11), TC levels (n = 11), and serum ALT (n = 10), AST (n = 8) levels in mice fed an HFD. **g** Glucose tolerance tests (n = 8) and **h** insulin tolerance tests (n = 7) were conducted. (i) Representative western blot images demonstrating the insulin-stimulated phosphorylation of AKT in livers. Mice were injected with either PBS (−) or insulin (+). **j**, **q** Eight-week-old mice were individually housed for 20 weeks with a HFHFD and intravenously injected with AAV8-GFP or AAV8-CHIP-GFP 10 weeks prior to sacrifice. **j** Representative livers of mice fed a HFHFD (left) and the calculated percentage of liver weight/body weight ratio (right) (n = 7). Grid cubes are 5 mm*5 mm. **k**–**m** Representative images of liver samples stained with Oil red O, f4/80 immunohistochemistry, and Sirius red. **n**, **o** qRT-PCR was used to quantify the relative transcript levels of inflammation and fibrosis genes in mouse liver samples (n = 7). **p**, **q** Hepatic TG (n = 7), TC (n = 7) levels, and serum ALT (n = 8), AST (n = 8) levels in mice fed an HFD. **r** Lysates of HFD-fed CON and OE mouse liver samples were immunoprecipitated with anti-STX17, followed by western blotting. **s** Representative images of immunofluorescence analyses of HFD-fed CON and OE mouse liver samples using confocal microscopy conducted using anti-STX17, anti-SNAP29, and anti-VAMP8 antibodies. Graphs indicate fluorescence intensities (white arrow). The error bars in (**g**) and (**h**) indicate SD. Data are presented as individual data points, mean ± SD is assessed by unpaired two-tailed *t*-test. GOI gene of interest.

accelerated activation of the insulin signaling pathway in the liver (Fig. 9i).

To further identify the therapeutic effects of CHIP on more severe forms of NAFLD, we fed the HFHFD to mice for 10 weeks, followed by intravenous injections of AAV8-GFP control (CON) or AAV8-CHIP-GFP (OE) and 10 weeks of feeding to induce NASH (Supplementary Fig. 15f). The mice did not exhibit any differences in weight gain, food intake, fructose water intake, or any physiological differences in adipose tissues and weights (Supplementary Fig. 17a-f); however, OE mice exhibited a lower percentage of LW/BW ratio (Fig. 9j) and an enhanced autophagic pathway, as evidenced by an increase in LC3-II and decrease in P62 levels (Supplementary Fig. 17g). Histochemical analyses revealed diminished steatosis, macrophage infiltration, and fibrosis in the livers of OE mice (Fig. 9k–m and Supplementary Fig. 15g, h), which was corroborated by mRNA analyses of the genes implicated in these pathways (Fig. 9n, o). Hepatic and serum analyses revealed decreased TG, TC, VLDL, FFA, HDL, LDL, β-HB, ALT, and AST (Fig. 9p, q and Supplementary Fig. 17h-j) levels. Moreover, STX17 ubiquitination and SNARE complex assembly were upregulated in OE mouse liver samples treated with HFD and HFHFD (Fig. 9r, s, and Supplementary Fig. 17k-l). These results suggest that CHIP overexpression in the liver suppresses HFD- or HFHFD-induced metabolic syndromes, possibly via upregulating STX17 ubiquitination and SNARE complex formation, which suggests CHIP as a plausible therapeutic target for liver-related metabolic diseases.

Discussion

This study provides strong evidence that non-degradative STX17 ubiquitination by CHIP has a protective effect against NAFLD progression. Unlike previously reported proteasomal degradation of STX17 under NAFLD, decreased expression of CHIP in hepatocytes did not affect the stability of STX17, but merely reduced SNARE complex formation. Mechanistically, hepatocyte-specific CHIP knockout decreased the K63- and K27-linked polyubiquitination of STX17, interaction with VAMP8, and lipophagy, which resulted in increased lipotoxicity under HFD. The damaged hepatocytes in HFD-fed H-KO mice seemed to affect the activation of HSCs and pro-inflammatory T cells, and M1 polarization of Kupffer cells, thereby promoting NASH-like phenotypes. On the contrary, AAV8-mediated CHIP overexpression in the liver increased K63- and K27-linked ubiquitination of STX17 and interaction with VAMP8, and attenuated NAFLD under HFD or HFHFD. It is notable that the interaction between STX17 and VAMP8 is dependent on the CHIP-mediated ubiquitination of STX17. It seems that the ubiquitination on STX17 might function as a ubiquitination scaffold that strengthens the interaction of STX17 with VAMP8.

Regarding multiple types of ubiquitination, this study supports the idea that different types of ubiquitination can occur simultaneously in one protein, and protein–protein interaction regulation via non-degradative ubiquitination can affect the prognosis of diseases. We suggest the dual roles of STX17 ubiquitination—degradative and non-degradative—under NAFLD. The decreased K63- and K27-linked polyubiquitination of STX17 by CHIP at the K198 site decreased interactions among the components of SNARE complexes under NAFLD. However, at the same time, the net-ubiquitination of STX17 increased during NAFLD, which led to proteasomal degradation of STX17. As there are 27 other lysine sites in STX17, the possibility of other regulators being involved in the ubiquitination process cannot be excluded. For example, the increased net-ubiquitination and proteasomal degradation of STX17 under NAFLD imply that other E3 ligases are involved in this process to possibly induce K48-linked-degradative-ubiquitination. Previous studies have supported the idea of non-degradative ubiquitination affecting the prognosis of various diseases[48–52]. CHIP is also known to play two major roles by mediating ubiquitination of its targets. One is to target the proteasome-dependent degradation and the other is to induce non-degradative ubiquitination for protein-protein interactions. For non-degradative ubiquitination, CHIP is known to promote non-degradative K63-linked ubiquitination on TAK1, LEF1, and AHR in cellular levels, which enhances interaction with NEMO, β-catenin, and CYP1A1, respectively[53–55]. In this study, we unveiled the distinctive function of CHIP in facilitating two different types of non-degradative ubiquitination, which are K63- and K27-linkages, targeting a single protein substrate at the physiological level for the first time. Overall, CHIP-mediated STX17 ubiquitination could provide a ubiquitination scaffold for SNARE complex formation by recruiting essential factors and other unknown adaptor proteins. Further studies are required to better elucidate whether other factors are involved in the underlying mechanisms.

Methods

Ethics statement

This research complies with all relevant ethical regulations. Tissue samples and medical records were acquired with the informed consent of all patients. The study was approved by the Institutional Review Board of Severance Hospital (IRB No. 4-2018-0537, Seoul, South Korea), and adhered rigorously to the ethical guidelines set forth in the Declaration of Helsinki. All mouse experiments were approved by the Institutional Animal Care and Use Committee of the Laboratory Animal Research Center of Yonsei University (IACUC-A-202212-1598-01).

Mice

CHIP-flox mice were purchased from EUCOMM and mated with *Albumin*-Cre mice (Jackson Laboratory) to generate hepatocyte-specific CHIP-knockout mice. C57BL./6 male mice were purchased from Nara Biotech (Republic of Korea). Mice tail samples were mixed with Tail Solution (500 mM Tris-HCl, 100 mM EDTA, 0.5% SDS, pH 8.0) and 0.1 mg/ml of Proteinase K (03115852001, Roche) at 55°C overnight. Mouse genomic DNA was extracted using phenol, chloroform, and isoamyl alcohol (p2026-050-80, Myungin Bio).

The primers used for *CHIP-flox* were 5′-TTCTGGCAGCCTGGACTCGATGGC-3′ and 5′-TCATAACTCTCCATCTCCAGCTGG-3′, which amplified an approximately 554-bp DNA fragment in $CHIP^{+/+}$ mice and a 700-bp DNA fragment in $CHIP^{flox/flox}$ mice. The primers used for *Albumin*-Cre were 5′-GTCGATGCAACGAGTGATGA-3′ and 5′-TCATCAGCTACACCAGAGAC-3′, which amplified an approximately 750-bp DNA fragment. Mice were housed in a 12 h light-dark cycle environment, wherein the ambient temperature was maintained at 21–23 °C and 40–50% humidity. Mice were fed a sterilized normal chow diet (NCD; protein, 20% kcal; fat, 4.5% kcal; carbohydrates, 61% kcal; Cargill Agri Purina Inc.) and sterilized tap water. To establish NAFLD, 8-week-old male mice were fed a high-fat diet (HFD; protein, 20% kcal; fat, 60% kcal; carbohydrate, 20% kcal; D12492, Research DIET Inc.) or a high-fat, high-fructose diet (HFHFD; HFD and 30% fructose in water, F0366, Samchun Chemicals). The mice used in all experiments were monitored daily. The weight, food intake, and fructose water intake of mice were measured twice a week. Only male mice were used in the experiments to avoid interference with pathophysiological functions by estrogens produced in female mice[56].

In-vivo gene delivery

Adeno-associated virus 8-mediated gene expression. AAV8-CMV-GFP and AAV8-EF1α-mCHIP-CMV-GFP were custom ordered (Virovek Inc.). CHIP and GFP were individually transcribed from different promoters to minimize the secondary effects. Eight-week-old C57BL./6 WT male mice were fed either a HFD for 8 weeks or a HFHFD for 10 weeks before AAV8 injection. 5E^11 vg of AAV8 was mixed in 200 μl of PBS and injected through the tail vein. After continuously being fed HFD or HFHFD for 8 and 10 weeks, the mice were sacrificed.

In-vivo-jet PEI transfection. Eight-week-old male mice were fed a HFD for 10 weeks to induce NAFLD. Four and one days prior to sacrifice, the mice were transfected with 50 μg/mouse of pcDNA3-HA, pcDNA3-HA-

mSTX17-WT, or pcDNA3-HA-mSTX17-K197R, respectively with in-vivo-jetPEI (101000030, Polyplus) through intravenous injection. Plasmids were mixed with in-vivo-jetPEI at an n/p ratio of 8 and incubated for 30 min at room temperature.

Histopathological analysis

Immunohistochemical analysis was conducted on 72 formalin-fixed paraffin-embedded (FFPE) human liver tissue specimens. Among these, 37 cases were diagnosed as NASH based on Kleiner et al.'s criteria[57], while 35 cases exhibited a healthy, normal liver, and were categorized as healthy controls. Samples with a NASH Activity Score (NAS) of 0 were categorized as healthy normal liver, whereas those with a NAS score >4 were identified as NASH liver. Immunohistochemistry was performed using the Dako EnVision+ System-HRP (Dako, Carpinteria, CA) as described previously[58]. Tissue sections (5 μm thick) were deparaffinized and rehydrated through graded alcohols, followed by heat-induced antigen retrieval using antigen retrieval buffer (pH6.0) (Dako). Subsequent to blocking the non-specific interactions, the sections were incubated with anti-CHIP rabbit polyclonal antibodies (HPA041222; dilution 1:2000; Millipore Sigma) or anti-STX17 rabbit polyclonal antibodies (PA5-40127; dilution 1:4000; Invitrogen) for 30 min at room temperature. The immunohistochemical staining images were assessed using Visiopharm software v2017.7.1.3885 (Visiopharm, Hørsholm, Denmark). The immunohistochemical score was represented as the percentage of positively stained cells, with a potential range of 0–100%. The final value was determined by calculating an average of the six regions of interest.

For mouse tissue samples, mouse adipose tissues and liver samples were dissected, fixed with 4% paraformaldehyde, and embedded in paraffin wax to create 4 μm thick section. The slices were stained with hematoxylin (03971, Sigma), eosin (318906, Sigma), Sirius red (ab246832, Abcam), and f4/80 antibody (ab111101, Abcam) as indicated. For Oil red O staining, mice livers were dissected and frozen in Tissue-Tek® O.C.T compound (4583, SAKURA) at −80 °C, and 10 μm thick sections were created. The slices were stained with Oil Red O (O0625, Sigma) diluted in 60% isopropanol (I0347, Samchun). The stained slides were examined using Lionheart XF, and the percentage of areas of interest was measured using ImageJ.

Transmission electron microscopy (TEM)

Mouse liver samples were dissected into 1mm3 pieces, fixed in 2% glutaraldehyde (G5882, Sigma) in 0.1 M phosphate buffer for 2 h at room temperature, and stored at 4 °C. For 1 M phosphate buffer, 68.4 ml of 1 M Na_2HPO_4 (795410, Sigma) and 31.6 ml of 1 M NaH_2PO_4 (RDD007, Sigma) were mixed with 900 ml of water. Fixed samples were then dehydrated with ascending grades of alcohol, embedded, and sectioned for TEM analysis. The sections were then observed under a transmission electron microscope (JEM-1400), operating at an accelerating voltage of 80 kV. Ten images per samples were randomly captured and used to quantify the number of autophagosomes or autolysosomes.

Quantitative RT-PCR

Mouse liver samples and HepG2 cells were mixed with TRIzol (BRL-15596-018, Invitrogen) and homogenized for RNA extraction. cDNA was synthesized using random hexamers (n8080127, Invitrogen), dNTP (4030, Takara), and PrimeScript reverse transcriptase (2680A, Takara). Quantitative RT-PCR (qRT-PCR) was conducted using the QuantiTect SYBR Green PCR kit (204143, Qiagen) and the following primers: mouse Tnf1, 5′-TCTTTGAGATCCATGCCGTTG-3′ and 5′-AGACCCTCACACTCAGATCA-3′; mouse Il1β, 5′-GACCTGTTCTTTGAAGTTGACG-3′ and 5′-CTCTTGTTGATGTGCTGCTG-3′; mouse f4/80, 5′-ATTCACTGTCTGCTCAACCG-3′ and 5′-GGAAGTGGATGGCATAGATGA-3′; mouse ccl5, 5′-GCTCCAATCTTGCAGTCGT-3′ and 5′-CCTCTATCCTAGCTCATCTCCA-3′; mouse col1a1, 5′-CATTGTGTATGCAGCTGACTTG-3′ and 5′-CGCAAAGAGTCTACATGTCTAGG-3′; mouse col1a2, 5′-AGTAACTTCGTGCCTAGCAAC-3′ and 5′-CATCAACACCATCTCTGCCT-3′; mouse tgfb, 5′-CCGAATGTCTGACGTATTGAAGA-3′ and 5′-GCGGACTACTATGCTAAAGAGG-3′; mouse α-sma, 5′-GAGCTACGAACTGCCTGAC-3′ and 5′-CTGTTATAGGTGGTTTCGTGGA-3′; mouse fasn, 5′-ACTCCTGTAGGTTCTCTGACTC-3′ and 5′-GCTCCTCGCTTGTCGTC-3′; mouse pparγ, 5′-TGCAGGTTCTACTTTGATCGC-3′ and 5′-CTGCTCCACACTATGAAGACAT-3′; mouse srebp1, 5′-GTCACTGTCTTGGTTGATG-3′ and 5′-CGAGATGTGCGAACTGGAC-3′; mouse scd1, 5′-AGCGGTACTCACTGGCA-3′ and 5′CCCTACGACAAGAACATTCAATC-3′; mouse atgl, 5′-GGAACCAAAGGACCTGATGA-3′ and 5′-ACTCCAACAAGCGGATGGT-3′; mouse cpt1β, 5′-CCTCCGAAAAGCACCAAAAC-3′ and 5′-GCTCCAGGGTTCAGAAAGTAC-3′; mouse hsl, 5′-CATGGCTCAACTCCTTCCTGGAAC-3′ and 5′-TTCAAGGTATCTGTGCCCAGTAAGCC-3′; mouse lpl, 5′-CCAGGATGCAACATTGGAGAAGC-3′ and 5′-GCAGGGAGTCAATGAAGAGATGAATG-3′; mouse tfeb, 5′-CCAGAAGCGAGAGCTCACAGAT-3′ and 5′-TGTGATTGTCTTTCTTCTGCCG-3′; mouse ulk1, 5′-CCAAGTCCCAAACACTGCT-3′ and 5′-CCAGGTAGACAGAATTAGCCAT-3′; mouse becn1, 5′-TTTCAGACTGGGTCGCTTG-3′ and 5′-CCATAGGGAACAAGTCGGTAC-3′; mouse atg5, 5′-AGTCAAGTGATCAACGAAATGC-3′ and 5′-ATTCCATGAGTTTCCGGTTGA-3′; mouse atg7, 5′-AGTCAAGTGATCAACGAAATGC-3′ and 5′-CTATGTGTCACGTCTCTAGCTC-3′; mouse lc3, 5′-GAGCGAGTTGGTCAAGATCA-3′ and 5′-CGTCTTCATCCTTCTCCTGTTC-3′; mouse p62, 5′-GCTGCCCTATACCCACATCT-3′ and 5′-CGCCTTCATCCGAGAAAC-3′; mouse lamp2, 5′-GATCACGATGTGCCTCTCTC-3′ and 5′- GCAAGTACCCTTTGAATCTGTC-3′; mouse mtor, 5′-TTGTGCTGAGATATGGAAGCAGGGTGAGGAGAAC-3′ and 5′-CTCCGCTCTTCCCGGCTACTCTAGCCTCCC-3′; HA, 5′-TACCCTTATGATGTGCCAGAT-3′ and 5′-CTCGAGCGGCCGCCAGTG-3′; mouse stx17, 5′-CAGCAGGAGAAGATTGACAGC-3′ and 5′-CTGCCAGCTTGTATTTTGCAG-3′; mouse 1KR, 5′-CAGCAGGAGAGGATTGACAGC-3′ and 5′-CTGCCAGCTTGTATTTTGCAG-3′. For HepG2 cells, qRT-PCR was conducted using the following primers: human tnf1, 5′-AACCTCCTCTCTGCCATCAA-3′ and 5′-GGAAGACCCCTCCCAGATAG-3′; human ccl5, 5′-CAGCACGTGGACCTCGCACA-3′ and 5′-GGCAGTGGGCGGGCAATGTA-3′; human il6, 5′-ACTCACCTCTTCAGAACGAATTG-3′ and 5′-CCATCTTTGGAAGGTTCAGGTTG-3′; human mcp1, 5′-CAGCCAGATGCAATCAATGCC-3′ and 5′-TGGAATCCTGAACCCACTTCT-3′; human col1a1, 5′-TTCTGTACGCAGGTGATTGG-3′ and 5′-GACATGTTCAGCTTTGTGGAC-3′; human col1a2, 5′-CCCAGCCAAGAACTGGTATAGG-3′ and 5′-GGCTGCCAGCATTGATAGTTTC-3′; human tgfb, 5′-GAAGTCACCCGCGTGCTAATGG-3′ and 5′-GTGTGTCCAGGCTCCAAATGTAGG-3′; human α-sma, 5′- CTGTTGTAGGTGGTTTCATGGA-3′ and 5′-AGAGTTACGAGTTGCCTGATG-3′; human f4/80, 5′-TTTCCTCGCCTGCTTCTTC-3′ and 5′-CCCCGTCTCTGTATTCAACC-3′; human il1β, 5′-ACGCTCCGGGACTCACAGCA-3′ and 5′-TGAGGCCCAAGGCCACAGGT-3′.

Hepatic and serum biochemistry

Primary hepatocyte isolation. Hepatocytes were isolated from non-fasted anesthetized male mice as previously described[59]. Cells were resuspended in low-glucose DMEM (D5546, Sigma) supplemented with 5% FBS (16000044, GIBCO) and 1% penicillin–streptomycin (SV30010, Hyclone) and seeded on 100-mm culture dishes (20100, SPL). After overnight incubation, hepatocytes were used for appropriate experiments.

Hepatic protein extraction. The liver samples were snap-frozen in liquid nitrogen for long-term storage. Samples were lysed in RIPA buffer (50 mM Tris-HCl, 150 mM NaCl, 1% NP-40, 0.1% SDS, and 0.5% sodium deoxycholate, pH 7.5) (Tris, TRS001-5, Biopure; SDS, SR2004-050-00, Biosesang; HCl, H0255, Samchun Chemicals; sodium deoxycholate, D6750, Sigma; NaCl, S2097, Samchun Chemicals) containing the following protease inhibitors, namely, 1 μg/ml of pepstatin A (P5318, Sigma), 2 μg/ml of leupeptin (L2884, Sigma), 2 μg/ml of

Aprotinin (A1153, Sigma), and 200 μM of phenylmethylsulfonyl fluoride (PMSF; P7626, Sigma), followed by homogenation. Lysates were centrifuged for 10 min at 15,928 × *g* and 4 °C. The supernatants were collected and used for the western blot analysis.

Hepatic TG and TC extraction. For TG extraction, 0.1 g of mouse liver samples was homogenized in 5% NP-40 (I8896, Sigma) in water, followed twice by heating to 95 °C and cooling to room temperature. The samples were centrifuged for 2 min at 13,572 × *g* and room temperature. The solubilized hepatic TG levels were measured using a Triglyceride Quantification Colorimetric/Fluorometric Kit (K622-100, Biovision). For TC extraction, 0.1 g of mouse liver samples were homogenized in 1 ml of chloroform:methanol (2:1, v/v) (chloroform, C2432, Sigma; methanol, 67-56-1, Duksan). The homogenized samples were mixed with 200 μl of water and centrifuged for 5 min at 376 × g. Cholesterol extracted from the mouse liver was measured using a Total Cholesterol and Cholesterol ester Colorimetric/Fluorometric Assay kit (K603-100, Biovision).

Serum analysis. Mice sera were collected via cardiac puncture, centrifuged for 30 min at 600 × g. Fasting serum TG, TC, AST, ALT, HDL, and LDL levels were measured using Cobas c502 from Roche (Cat no. 2076710732, 03039773190, 20764949322, 20764957322, 07528566190, and 07005717190, respectively). The serum FFA levels were measured using Shinyang (R1:1120301, R2:1120302). Serum VLDL levels were calculated by dividing the measured serum TG levels by 5. The serum insulin levels were measured using a rat/mouse insulin ELISA (EZRMI-13K, Sigma) according to the recommended protocol. For serum β-hydroxybutyrate, mice sera were placed in a 10 K MWCO protein concentrator (88513, Thermo), deproteinized via centrifugation for 10 min at 15,928 × *g* and 4 °C, and measured using a beta-HB assay kit (ab83390, Abcam).

Glucose tolerance test and insulin tolerance test. A HFD was fed for 20 weeks to WT and H-KO mice, and for 16 weeks to CON and OE mice, and tested after an overnight fast. The glucose tolerance test (GTT) was conducted by administering oral glucose (G8769, Sigma) at a dose of 1 g/kg. The blood glucose levels were analyzed at 0-, 15-, 30-, 60-, and 120-min post-injection using Handok–Barozen blood glucose test strips. For the insulin tolerance test (ITT), insulin (I9278, Sigma) stimulation was administered through intraperitoneal insulin injection at a dose of 0.75 U/kg (final volume was 200 μl). The blood glucose levels were analyzed at 0-, 15-, 30-, 60-, 120-, and 150-min post-injection. The liver samples were collected 15 min after insulin injection and snap-frozen for western blot analysis.

Bulk RNAseq and snRNAseq analysis. Eight-week-old WT and H-KO mice were fed an NCD or HFD for 20 weeks and subsequently dissected for liver samples. The samples were snap frozen in liquid nitrogen, transported to GININUS Inc., and stored in liquid nitrogen. Total RNA-seq was performed for bulk RNAseq analysis, and chromium single cell 3′ gene expression was performed for snRNAseq analysis. For snRNAseq, 10X fastq were merged with cellranger-6.1.2, and processed with R v4.3.0, Seurat V4.3.0. Cells with 200<nFeature<7500 and perncent.mito<25% were used for analysis. The top 30 dimensions were used to plot the variability between cells in a two-dimensional diagram using the UMAP procedure to reduce data dimensionality. Cells were clustered into subpopulations according to the same dimensions using the "FindClusters" function with a 0.8 resolution. The subclustering of HSCs was created from the "Subset" function of Seurat. Dimensional reduction, UMAP, and clustering (resolution = 1.0) were performed as described above. Cell types were assigned manually to each cluster based on known expression of signature genes.

Differential expression and enrichment analysis. Differential gene expression testing was performed using the "FindMarkers" function in Seurat. DEGs were filtered using a log fold change of 0.25 and adjusted *p*-value of 0.05. Enrichment analysis of DEG functions was conducted using the ClusterProfiler (v3.12.0) package. GSEA was performed using the genekitr package with DEGs from each cell type based on Gene Ontology terms pathways.

Cell lines and transfection

Cell culture. HepG2 (a human hepatoblastoma cell line; HB-8065) and 293FT (a human embryonic kidney cell line; CRL-3216) cells were acquired from the American Type Culture Collection (ATCC) and grown in Dulbecco's modified Eagle's medium (DMEM; Hyclone) containing 10% fetal bovine serum (FBS; 16000044, GIBCO) and 1% penicillin–streptomycin (SV30010, Hyclone). All cell lines were protected from mycoplasma infection by treatment with Plasmocin™ (InvivoGen). 100 nM of Bafilomycin A1 (19-148, Sigma) was used to inhibit autophagosome and lysosome fusion.

For FFA-induced lipid accumulation, 0.282 g of oleic acid (OA; O1008, Sigma) was mixed with 1 ml of 0.1 M NaOH (221465, Sigma) by heating at 70 °C for 3 h to create sodium oleate. Sodium oleate was mixed with 9 ml of 1% bovine serum albumin (BSA; A0100-010, GenDEPOT) in water, mixed vigorously for 10 s and incubated at 55 °C for 30 min to make 0.1 M oleic acid-albumin. BSA (1%) in water was used as the control. OA (0.1 M) was diluted to 1 mM in serum-free DMEM and used to treat the HepG2 cells for overnight.

Plasmids. Information on all CHIP-related plasmids used in this study can be found in ref. 60. pT7T3D-STX17, pCMV-SPORT6-SNAP29, and pOTB7-VAMP8 were purchased from the Korea Human Gene Bank and cloned into the pcDNA3-HA, pcDNA3-FLAG, and pMSCV-FLAG vectors. The shRNA sequence of STX17 was obtained from Sigma and cloned into the pLKO.1-puro vector. RFP-GFP-LC3 was provided by H. W. Lee (Yonsei University, Korea)[61].

In-vitro transfection and virus infection. For transient transfection, plasmids were incubated with serum-free DMEM and PEI (408727, Sigma) for 20 min and then incubated with either HepG2 or 293FT cells overnight.

For stable transfection, pBABEpuro-CHIP, pBABEpuro-CHIP-H260Q, pBABEpuro-K30A, pMSCV-FLAG-STX17, pMSCV-FLAG-STX17-1KR, pMSCV-FLAG-STX17-3KR, and pMSCV-FLAG-STX17-4KR were transfected into 293FT cells using viral packaging vectors pVSV-G and Gag-pol. pLKO.1-puro-shCHIP#3 and #4 and pLKO.1-puro-shSTX17 #2, and #4 were transfected into 293FT cells with virus packaging vectors pRSV-REV, pMD2.G, and pMDLg/pRRE. The viruses were filtered through a 0.45 μm filter (slhp033rs, Millipore) and infected to HepG2 cells with polybrene (sc-134220, Santacruz).

Biochemical analysis

Immunoprecipitation assays. Cells were collected with cold PBS (LB-201-02, Welgene) and lysed using DISC lysis buffer (50 mM Tris-HCl, 150 mM NaCl, 1% Triton X-100, 1 mM EDTA, and 10% glycerol, pH 7.5) (EDTA, 15575020, Thermo; Triton X-100, X100, Sigma; glycerol, G0269, Samchun Chemicals) containing the following protease inhibitors, namely, 1 μg/ml of pepstatin A, 2 μg/ml of leupeptin, 2 μg/ml of aprotinin, and 200 μM of PMSF. The cells were incubated with appropriate antibodies at 4 °C overnight. Lysates were then incubated with 20 μl of protein G agarose bead (11243233001, Sigma) for 2 h. Proteins were eluted by boiling in Laemmli sample buffer and used for western blot analysis.

Ubiquitination assays. Cells were collected in cold PBS containing 5 mM *N*-ethylmaleimide (NEM; E3876, Sigma) and lysed by boiling for 10 min in PBS containing 1% SDS, and 5 mM NEM. The lysates were

immunoprecipitated in DISC buffer (final concentration of 0.1% SDS). Lysates were centrifuged for 10 min at 15,928 × g and 4 °C, and the supernatant was collected for the immunoprecipitation assay.

Western blot analysis. Protein concentrations were quantified using a bicinchoninic acid protein assay kit (23225, Thermo Fisher Scientific). Mouse tissue protein extracts or cells were mixed with Laemmli sample buffer and boiled for 10 min. After separation by SDS-PAGE, the proteins were transferred onto nitrocellulose membranes (10600003, Amersham). Subsequently, membranes were sequentially incubated with specific primary antibodies for CHIP (C-10) (1:2000, sc-133083, Santa Cruz), CHIP (1:2000, 2080, Cell signaling technology), GAPDH (1:5000, 5714, Cell signaling technology), P62 (1:2000, 610832, BD transduction), LC3 (1:2000, L8918, Sigma), β-ACTIN (1:5000, A5316, Sigma), FLAG (1:2000, A8592, Sigma), HA (1:2000, sc-7392, Santa Cruz), AKT1 (2H10) (1:1000, 2967, Cell signaling technology), phosphor-AKT1 (S473) (1:1000, 9271, Cell signaling technology), STX17 (1:1000, ab229646, Abcam), SNAP29 (1:1000, sc-390602, Santa Cruz), Ub (1:1000, 14049, Cell signaling technology), K63-linked Ub (1:1000, 5621, Cell signaling technology), K27-linked Ub (1:1000, ab181537, Abcam), ULK1 (1:1,000, 8054, Cell signaling technology), mTOR (1:1000, 2983, Cell signaling technology), BECN1 (1:11000, 3738S, Cell signaling technology), ATG3 (1:1000, M133-3, MBL), ATG5 (1:1000, M153-3, MBL), AMPKα (1:1000, 2603, Cell signaling technology), VPS34 (1:1000, 4263, Cell signaling technology), LAMP2A (1:1000, ab125068, Abcam), c-Myc (9E10) (1:5000, sc-40, Santa Cruz), and GFP (1:2000, sc8334, Santa Cruz) at 4 °C overnight and detected with Vilber Fusion Imaging System.

Fluorescence analysis

Nile red and BODIPY 493/503 staining. HepG2 cells were seeded into sterilized 12-well plates containing cover glasses (12 mm; HAS-011520, Hyunil Lab-Mate) and incubated for 1 day. After the cells were attached to the surface of the cover glass, the culture medium was discarded and replaced with 1 mM OA in serum-free DMEM. The next day, the cover glass was isolated from the 12-well plate and used for Nile red staining. The cells were fixed with 4% paraformaldehyde for 10 min, incubated with Hoechst 33342 (1:1000, H3570, Invitrogen) for 10 min. The cells were washed twice with 60% isopropanol (34863, Sigma-Aldrich) in water. The cells were finally stained with 1 μg/ml of Nile Red (19123, Sigma) in 60% isopropanol for 30 min at 37 °C in the dark, and mounted by applying the gel mounting solution (M01, Biomeda). For BODIPY 493/503 staining, after fixing in 4% paraformaldehyde, the cells were stained with 1 μM BODIPY 493/503 (D3922, Invitrogen) in PBS for 15 min at 37 °C in the dark and mounted by applying the gel mounting solution. The cells were analyzed using a Lionheart FX and Zeiss Zen LSM980 confocal microscope.

Immunofluorescence analysis. FFPE-liver samples were deparaffinized and rehydrated. Heat-induced antigen retrieval was performed with citrate buffer (10 mM sodium citrate, 0.05% TWEEN-20, pH 6.0) (sodium citrate, S1804, Sigma; TWEEN-20, 0777, Amresco), and the samples were incubated with specific Alexafluor-conjugated antibodies against STX17 (1:50, sc518187AF594, Santa Cruz), SNAP29 (1:50, sc390602AF546, Santa Cruz), VAMP8 (1:50, ab202828, Abcam), and CHIP (1:50, ab310058, Abcam). Hoechst 33342 (1:1000, H3570, Invitrogen) was added just before mounting.

HepG2 cells were seeded into sterilized 12-well plates containing cover glasses (12 mm; HAS-011520, Hyunil Lab-Mate) and incubated for 1 day. The cells were then fixed in 4% paraformaldehyde for 10 min and incubated with 0.5% Triton X-100 (X100, Sigma) for 10 min. Antibodies specific to CHIP, STX17, HA, and FLAG were diluted to 1:200 in 2.5% BSA in PBS and incubated overnight at 4 °C. The cells were then incubated with Alexa 594 goat anti-rabbit antibody (1:400, A11012, Thermo) or Alexa 488 goat anti-mouse IgG (1:400, A28175, Thermo) for 1 h at room temperature. The cover glasses were mounted on glass slides and examined under a Zeiss Zen LSM980 confocal microscope.

RFP-GFP-LC3 assay. HepG2 cells were seeded into sterilized 12-well plates containing cover glasses (12 mm) and incubated for 1 day. The RFP-GFP-LC3 plasmids were then transfected into cells using PEI. The following day, the cells were incubated with 1 mM OA in serum-free DMEM overnight. The cells were fixed with 4% paraformaldehyde for 10 min and analyzed using Lionheart FX. The percentage of red and yellow puncta per cell was measured using Image J.

Statistics and reproducibility

All statistical tests were two-sided, and the values were expressed as means with 95% confidence intervals. Statistically significant differences between the groups were examined using unpaired two-tailed *t*-tests. The quantification of ubiquitination in Fig. 7 was examined using paired two-tailed *t*-tests. Data were assessed by using the GraphPad Prism software (version 7; GraphPad Software Inc.). Statistical analyses of RNAseq results were performed using the Wilcox test in R version 4.3.0. Results from representative experiments were obtained from at least three independent experiments. Statistical significance is indicated in the figure legends.

Reporting summary

Further information on research design is available in the Nature Portfolio Reporting Summary linked to this article.

Data availability

The corresponding author can provide the datasets used in this study upon reasonable request. The transcriptomic sequencing data are available through the National Center for Biotechnology Information Sequence Read Archive (SRA) under accession code PRJNA1137118. Source data are provided with this paper.

References

1. Wai-Sun Wong, V., Ekstedt, M., Lai-Hung Wong, G. & Hagstrom, H. Changing epidemiology, global trends and implications for outcomes of NAFLD. *J. Hepatol.* **79**, 842–852 (2023).
2. Khan, R. S., Bril, F., Cusi, K. & Newsome, P. N. Modulation of insulin resistance in nonalcoholic fatty liver disease. *Hepatology* **70**, 711–724 (2019).
3. Rinella, M.E. et al. A multi-society Delphi consensus statement on new fatty liver disease nomenclature. *J. Hepatol.* **78**, 1966–1986 (2023).
4. Shah, P. A., Patil, R. & Harrison, S. A. NAFLD-related hepatocellular carcinoma: the growing challenge. *Hepatology* **77**, 323–338 (2023).
5. Huang, D. Q. et al. Changing global epidemiology of liver cancer from 2010 to 2019: NASH is the fastest growing cause of liver cancer. *Cell Metab.* **34**, 969–977 e962 (2022).
6. Younossi, Z.M., Zelber-Sagi, S., Henry, L. & Gerber, L.H. Lifestyle interventions in nonalcoholic fatty liver disease. *Nat. Rev. Gastroenterol. Hepatol.* **20**, 708–722 (2023).
7. Ferguson, D. & Finck, B. N. Emerging therapeutic approaches for the treatment of NAFLD and type 2 diabetes mellitus. *Nat. Rev. Endocrinol.* **17**, 484–495 (2021).
8. Cai, J., Zhang, X. J. & Li, H. Progress and challenges in the prevention and control of nonalcoholic fatty liver disease. *Med. Res. Rev.* **39**, 328–348 (2019).
9. Zadoorian, A., Du, X. & Yang, H. Lipid droplet biogenesis and functions in health and disease. *Nat. Rev. Endocrinol.* **19**, 443–459 (2023).
10. Zhang, H. et al. Dynamic MTORC1-TFEB feedback signaling regulates hepatic autophagy, steatosis and liver injury in long-term nutrient oversupply. *Autophagy* **14**, 1779–1795 (2018).

11. Yamamoto, H., Zhang, S. & Mizushima, N. Autophagy genes in biology and disease. *Nat. Rev. Genet.* **24**, 382–400 (2023).
12. Yim, W. W. & Mizushima, N. Lysosome biology in autophagy. *Cell Discov.* **6**, 6 (2020).
13. Itakura, E., Kishi-Itakura, C. & Mizushima, N. The hairpin-type tail-anchored SNARE syntaxin 17 targets to autophagosomes for fusion with endosomes/lysosomes. *Cell* **151**, 1256–1269 (2012).
14. Ma, M., Xie, W. & Li, X. Identification of autophagy-related genes in the progression from non-alcoholic fatty liver to non-alcoholic steatohepatitis. *Int J. Gen. Med.* **14**, 3163–3176 (2021).
15. Tripathi, M. et al. Vitamin B(12) and folate decrease inflammation and fibrosis in NASH by preventing syntaxin 17 homocysteinylation. *J. Hepatol.* **77**, 1246–1255 (2022).
16. Cheng, X. et al. Pacer is a mediator of mTORC1 and GSK3-TIP60 signaling in regulation of autophagosome maturation and lipid metabolism. *Mol. Cell* **73**, 788–802 e787 (2019).
17. Li, Y. et al. Loss of splicing factor SRSF3 impairs lipophagy through ubiquitination and degradation of syntaxin17 in hepatocytes. *J. Lipid Res* **64**, 100342 (2023).
18. Zhang, S., Hu, Z. W., Mao, C. Y., Shi, C. H. & Xu, Y. M. CHIP as a therapeutic target for neurological diseases. *Cell Death Dis.* **11**, 727 (2020).
19. Seo, J., Han, S. Y., Seong, D., Han, H. J. & Song, J. Multifaceted C-terminus of HSP70-interacting protein regulates tumorigenesis via protein quality control. *Arch. Pharm. Res.* **42**, 63–75 (2019).
20. Zeng, Z. C. et al. METTL3 protects METTL14 from STUB1-mediated degradation to maintain m(6) A homeostasis. *EMBO Rep.* **24**, e55762 (2023).
21. Zhang, P. et al. Ubiquitin ligase CHIP regulates OTUD3 stability and suppresses tumour metastasis in lung cancer. *Cell Death Differ.* **27**, 3177–3195 (2020).
22. Tang, D. E. et al. STUB1 suppresseses tumorigenesis and chemoresistance through antagonizing YAP1 signaling. *Cancer Sci.* **110**, 3145–3156 (2019).
23. Ullah, K. et al. The E3 ubiquitin ligase STUB1 attenuates cell senescence by promoting the ubiquitination and degradation of the core circadian regulator BMAL1. *J. Biol. Chem.* **295**, 4696–4708 (2020).
24. Han, S. Y. et al. Molecular chaperone HSP90 is necessary to prevent cellular senescence via lysosomal degradation of p14ARF. *Cancer Res.* **77**, 343–354 (2017).
25. Tawo, R. et al. The ubiquitin ligase CHIP integrates proteostasis and aging by regulation of insulin receptor turnover. *Cell* **169**, 470–482 e413 (2017).
26. Qiu, J., Shu, C., Li, X. & Zhang, W. C. PAQR3 depletion accelerates diabetic wound healing by promoting angiogenesis through inhibiting STUB1-mediated PPARgamma degradation. *Lab Investig.* **102**, 1121–1131 (2022).
27. Kim, J. H. et al. C-terminus of HSC70-interacting protein (CHIP) inhibits adipocyte differentiation via ubiquitin- and proteasome-mediated degradation of PPARgamma. *Sci. Rep.* **7**, 40023 (2017).
28. Kim, S.-M., Grenert, J. P., Patterson, C. & Correia, M. A. CHIP −/−-mouse liver: adiponectin-AMPK-FOXO-activation overrides CYP2E1-elicited JNK1-activation, delaying onset of NASH: therapeutic implications. *Sci. Rep.* **6**, 29423 (2016).
29. Schisler, J. C. et al. CHIP protects against cardiac pressure overload through regulation of AMPK. *J. Clin. Investig.* **123**, 3588–3599 (2013).
30. Sha, Y., Rao, L., Settembre, C., Ballabio, A. & Eissa, N. T. STUB1 regulates TFEB-induced autophagy-lysosome pathway. *EMBO J.* **36**, 2544–2552 (2017).
31. Lizama, B. N. et al. Neuronal preconditioning requires the mitophagic activity of C-terminus of HSC70-interacting protein. *J. Neurosci.* **38**, 6825–6840 (2018).
32. Dai, Q. et al. CHIP activates HSF1 and confers protection against apoptosis and cellular stress. *EMBO J.* **22**, 5446–5458 (2003).
33. Sahara, N. et al. In vivo evidence of CHIP up-regulation attenuating tau aggregation. *J. Neurochem* **94**, 1254–1263 (2005).
34. Arendt, B. M. et al. Altered hepatic gene expression in nonalcoholic fatty liver disease is associated with lower hepatic n-3 and n-6 polyunsaturated fatty acids. *Hepatology* **61**, 1565–1578 (2015).
35. Loft, A. et al. Liver-fibrosis-activated transcriptional networks govern hepatocyte reprogramming and intra-hepatic communication. *Cell Metab.* **33**, 1685–1700 e1689 (2021).
36. Yamamoto, A. et al. Bafilomycin A1 prevents maturation of autophagic vacuoles by inhibiting fusion between autophagosomes and lysosomes in rat hepatoma cell line, H-4-II-E cells. *Cell Struct. Funct.* **23**, 33–42 (1998).
37. Xu, W. et al. Chaperone-dependent E3 ubiquitin ligase CHIP mediates a degradative pathway for c-ErbB2/Neu. *Proc. Natl Acad. Sci. USA* **99**, 12847–12852 (2002).
38. Kimura, S., Noda, T. & Yoshimori, T. Dissection of the autophagosome maturation process by a novel reporter protein, tandem fluorescent-tagged LC3. *Autophagy* **3**, 452–460 (2007).
39. Zhang, D. D. et al. Nuciferine downregulates Per-Arnt-Sim kinase expression during its alleviation of lipogenesis and inflammation on oleic acid-induced hepatic steatosis in HepG2 cells. *Front. Pharm.* **6**, 238 (2015).
40. Wiriyakulsit, N., Keawsomnuk, P., Thongin, S., Ketsawatsomkron, P. & Muta, K. A model of hepatic steatosis with declined viability and function in a liver-organ-on-a-chip. *Sci. Rep.* **13**, 17019 (2023).
41. Nakamura, A. & Terauchi, Y. Lessons from mouse models of high-fat diet-induced NAFLD. *Int. J. Mol. Sci.* **14**, 21240–21257 (2013).
42. Zamani, M., Taher, J. & Adeli, K. Complex role of autophagy in regulation of hepatic lipid and lipoprotein metabolism. *J. Biomed. Res.* **31**, 377–385 (2017).
43. McCarthy, C.G. et al. Ketone body beta-hydroxybutyrate is an autophagy-dependent vasodilator. *JCI Insight* **6**, e149037 (2021).
44. Tsamos, G. et al. Therapeutic potentials of reducing liver fat in non-alcoholic fatty liver disease: close association with type 2 diabetes. *Metabolites* **13**, 517 (2023).
45. Nazeer, B. et al. Emerging role of lipophagy in liver disorders. *Mol. Cell Biochem.* **479**, 1–11 (2024).
46. Li, Y. et al. Decoding three distinct states of the Syntaxin17 SNARE motif in mediating autophagosome-lysosome fusion. *Proc. Natl Acad. Sci. USA* **117**, 21391–21402 (2020).
47. Swatek, K. N. & Komander, D. Ubiquitin modifications. *Cell Res.* **26**, 399–422 (2016).
48. Cao, L., Liu, X., Zheng, B., Xing, C. & Liu, J. Role of K63-linked ubiquitination in cancer. *Cell Death Discov.* **8**, 410 (2022).
49. Madiraju, C., Novack, J. P., Reed, J. C. & Matsuzawa, S. I. K63 ubiquitination in immune signaling. *Trends Immunol.* **43**, 148–162 (2022).
50. Tracz, M. & Bialek, W. Beyond K48 and K63: non-canonical protein ubiquitination. *Cell Mol. Biol. Lett.* **26**, 1 (2021).
51. Zhou, Q. & Zhang, J. K27-linked noncanonic ubiquitination in immune regulation. *J. Leukoc. Biol.* **111**, 223–235 (2022).
52. van Huizen, M. & Kikkert, M. The role of atypical ubiquitin chains in the regulation of the antiviral innate immune response. *Front. Cell Dev. Biol.* **7**, 392 (2019).
53. Liu, Y. et al. CHIP promotes the activation of NF-kappaB signaling through enhancing the K63-linked ubiquitination of TAK1. *Cell Death Discov.* **7**, 246 (2021).
54. Liu, Y. et al. CHIP promotes Wnt signaling and regulates Arc stability by recruiting and polyubiquitinating LEF1 or Arc. *Cell Death Discov.* **7**, 5 (2021).
55. Wang, W., Xiang, T., Yang, Y., Wang, Z. & Xie, J. E3 ubiquitin ligases STUB1/CHIP contributes to the Th17/Treg imbalance via the ubiquitination of aryl hydrocarbon receptor in rheumatoid arthritis. *Clin. Exp. Immunol.* **209**, 280–290 (2022).

56. Palmisano, B. T., Zhu, L. & Stafford, J. M. Role of estrogens in the regulation of liver lipid metabolism. *Adv. Exp. Med. Biol.* **1043**, 227–256 (2017).
57. Kleiner, D. E. et al. Design and validation of a histological scoring system for nonalcoholic fatty liver disease. *Hepatology* **41**, 1313–1321 (2005).
58. Lee, M. S. et al. PI3K/AKT activation induces PTEN ubiquitination and destabilization accelerating tumourigenesis. *Nat. Commun.* **6**, 7769 (2015).
59. Charni-Natan, M. & Goldstein, I. Protocol for primary mouse hepatocyte isolation. *STAR Protoc.* **1**, 100086 (2020).
60. Seo, J. et al. CHIP controls necroptosis through ubiquitylation- and lysosome-dependent degradation of RIPK3. *Nat. Cell Biol.* **18**, 291–302 (2016).
61. Roh, J. I. et al. Hexokinase 2 is a molecular bridge linking telomerase and autophagy. *PLoS One* **13**, e0193182 (2018).

Acknowledgements

This study was supported by a grant from the National Research Foundation of Korea (NRF), funded by the Ministry of Science, ICT, and Future planning (MSIP) (No. NRF-2015R1A3A206658133), in part by NRF grant funded by the Korean government (MSIT) (No. NRF-2020R1A5A1019023), in part by a NRF grant (No. NRF-2023K2A9A2A1005899911), in part by a NRF grant (No. RS-2024-00346972), and in part by the Brain Korea 21 (BK21) FOUR program.

Author contributions

H.R. conceptualized the study, designed and performed all experiments, analyzed data and wrote the manuscript. S.K. prepared materials and performed dissection of mice. S.H.L. performed analyses of RNAseq data. S.U.K., J.W.K., S.H.P., F.E. and J-Y.C. collected human liver samples and performed histopathologic experiments. J.S. directed the experiments and revised the manuscript. All authors approved the final version of the manuscript.

Competing interests

The authors declare no competing interests.

Additional information

Supplementary information The online version contains supplementary material available at https://doi.org/10.1038/s41467-024-53002-0.

Correspondence and requests for materials should be addressed to Jaewhan Song.

Peer review information *Nature Communications* thanks Chang-Hoon Woo and the other, anonymous, reviewer(s) for their contribution to the peer review of this work. A peer review file is available.